aza-BODIPY synthesis towards vis/NIR functional chromophores based on a Schiff base forming reaction protocol using lactams and heteroaromatic amines

Shimizu, Soji
Department of Chemistry and Biochemistry, Graduate School of Engineering, Kyushu University

出版情報：Chemical Communications. 55 (60), pp.8722-8743, 2019-06-24. Royal Society of Chemistry (RSC)
バージョン：
権利関係：

ChemComm

Feature Article

aza-BODIPY synthesis towards vis/NIR functional chromophores based on a Schiff base forming reaction protocol using lactams and heteroaromatic amines

Received 00th January 20xx,
Accepted 00th January 20xx

DOI: 10.1039/x0xx00000x

Soji Shimizu*[a,b]

aza-BODIPY has been a class of heteroatom-containing BODIPY analogues targeting the near infrared (NIR) chromophore and fluorophore. As a synthetic strategy towards aza-BODIPY structures, we have, recently, developed a Schiff base forming reaction using readily available lactams and heteroaromatic amines. Absorption and fluorescence of a series of compounds cover the whole range of the ultraviolet (UV)/visible (vis)/NIR regions. In addition, some compounds exhibit solid state emission, aggregation-induced emission enhancement, tunable fluorescence in the vis/NIR regions and non-linear optical properties. Furthermore, simple dimerization of aza-BODIPY chromophores caused unusual panchromatic absorption, whereas in combination with N-confused porphyrin skeleton, multi-state NH tautomerism was achieved. In this Feature Article, wide applicability of this Schiff base forming reaction and optical and electrochemical properties of aza-BODIPY analogues thus synthesized are summarized including recent applications, such as bioimaging, photothermal cancer therapy and organic photovoltaics.

1. Introduction

4,4-Difluoro-4-bora-3*a*,4*a*-diaza-*s*-indacene (BODIPY), a boron difluoride complex of dipyrrin,[1–3] has been a class of functional chromophores and fluorophores in the ultraviolet (UV)/visible (vis) regions. Due to the intense absorption and environmentally insusceptible fluorescence properties, BODIPY has been widely investigated in a variety of research fields, such as bioimaging,[4–6] chemosensors,[7] laser dyes,[8] sensitizers for photodynamic therapy[9] and optoelectronic materials like light-emitting diodes[10] and organic photovoltaics.[11] BODIPY has also been frequently utilized to create multi-chromophore systems for the study of artificial photosynthetic models[12] because of the high donor ability. In these application researches, there has, recently, been an urgent need to develop near infrared (NIR) chromophores. For example, fluorescence imaging in the NIR window (650–1350 nm) can afford high resolution and deep tissue penetration as background noise from tissue scattering is reduced. As for organic photovoltaics, panchromatic absorption in the vis/NIR region is ideal to harvest solar energy. Because conventional BODIPY exhibits its absorption and fluorescence at around 500 and 520 nm, respectively, much effort has been devoted to shift them into the NIR region mainly based on three modification strategies, 1. peripheral annulation to expand π-conjugation, 2. introduction of push or pull substituents and 3. heteroatom substitution (Fig. 1).[5,13] Among these structurally modified BODIPY analogues, aza-BODIPY as a heteroatom substituted analogue, in which a methine carbon atom at *meso*-position is replaced with an imino nitrogen atom, is known to exhibit its absorption and fluorescence in a wavelength region longer than 650 nm. Although the ligand structure of aza-BODIPY, aza-dipyrrin, was reported for the first time more than 70 years ago,[14] it remained unstudied for a long time until O'Shea et al. repeated the synthesis and revealed the drastic bathochromic shift of absorption and fluorescence of aza-BODIPY from those of BODIPY couterparts.[15] Since that time, an intensive research has been focused on its potential application in bioimaging, sensor and therapeutics.[16]

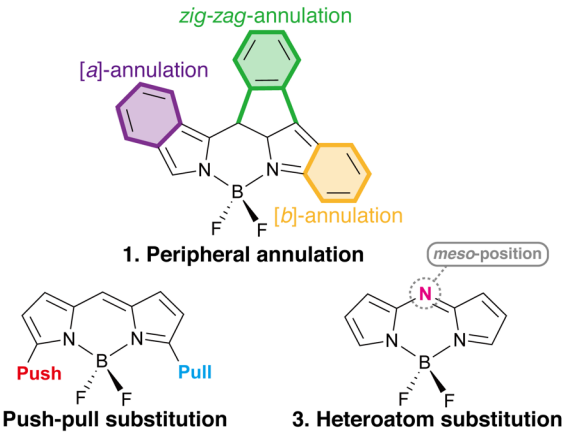

Fig. 1. Structural modification strategies towards creation of NIR BODIPY analogues.

[a] *Department of Chemistry and Biochemistry, Graduate School of Engineering, Kyushu University, Fukuoka 819-0395, Japan. E-mail: ssoji@cstf.kyushu-u.ac.jp Fax: +81 92 802 2866*
[b] *Center for Molecular Systems (CMS), Kyushu University, Fukuoka 819-0395, Japan.*

The significant red-shifts of absorption and fluorescence of aza-BODIPY from those of regular BODIPY can be ascribed to efficient stabilization of the lowest unoccupied molecular orbital (LUMO) due to the higher electronegativity of nitrogen than carbon at the *meso*-position. Large molecular orbital (MO) coefficients locate on the *meso*-position in the LUMO, whereas the highest occupied molecular orbital (HOMO) has a node at this position (Fig. 2). Therefore, the LUMO is more significantly stabilized compared to the HOMO. Since the main absorption of BODIPY and aza-BODIPY consists of a HOMO–LUMO transition, aza-BODIPY exhibits longer absorption than BODIPY because of the smaller HOMO–LUMO gap (⊿HL).

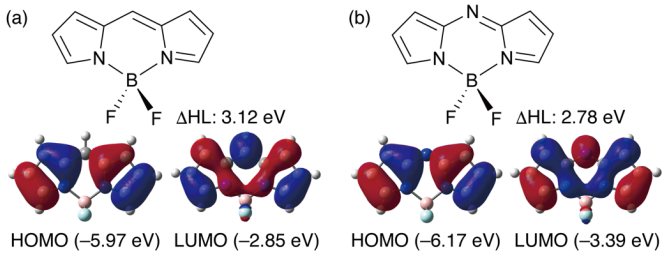

Fig. 2. Structures and frontier MOs of (a) BODIPY and (b) aza-BODIPY. MOs and their energies were calculated at the B3LYP/6-31G(d) level.

Owing to the pioneering investigations by several groups, three major synthetic routes of aza-BODIPY have been established to date (Scheme 1). In the first two methods, a nitroso-pyrrole generated *in situ* from pyrrole or 1,3-diaryl-4-nitrobutan-1-one is a key intermediate to synthesize an aza-dipyrrin structure, which is, then, converted to aza-BODIPY by BF_2 complexation (Scheme 1a and 1b).[15–18] The other method was developed based on the phthalocyanine synthesis, using phthalonitrile and a Grignard reagent (Scheme 1c).[19] In the proposed reaction mechanism, an 1-aryl-1*H*-isoindole-3-imine intermediate is condensed to form an aza-dipyrrin structure.[20] Recently, Cammidge et al. reported the synthesis of aza-BODIPY derivatives from aminoisoindoline derived from bromoamidine and arylacetylene (Scheme 2).[21]

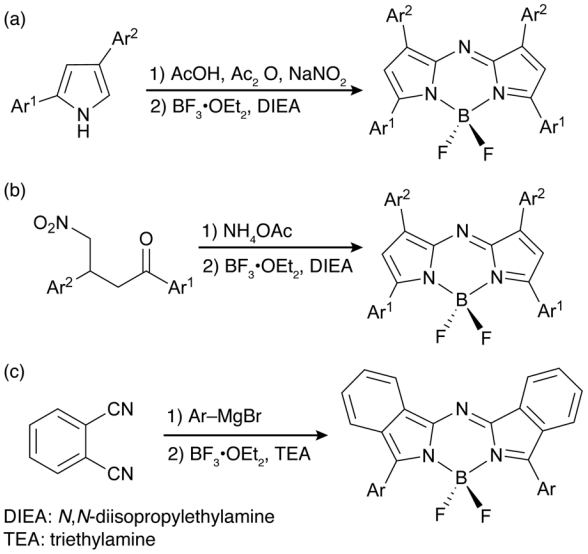

Scheme 1. Representative synthetic methods of aza-BODIPY.

Although various types of aza-BODIPYs have been synthesized, pyrrole derivatives and intermediates bearing substituents at 2-position or 2,4-positions are indispensable for the reported synthetic methods. To broaden structural scope of aza-BODIPY, recently our group attempted to develop the fourth synthetic method.

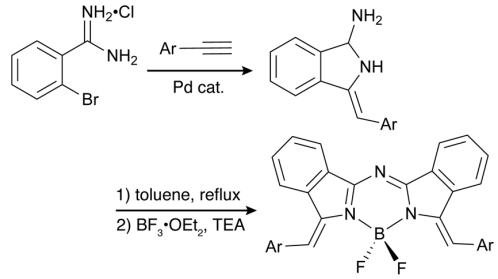

Scheme 2. Synthesis of aza-BODIPY derivative via aminoisoindoline.

As a new synthetic method, we developed a Schiff base forming reaction of lactam and heteroaromatic amine. After several reaction conditions were examined, we finally found that a combination of titanium tetrachloride ($TiCl_4$) and base, which was utilized for the synthesis of so-called Nindigo from indigo and aniline,[22] successfully activated the lactam moiety for imine-formation to provide an aza-dipyrrin skeleton. After optimization of reaction conditions, we noticed that using triethylamine as a base, aza-BODIPY analogues were synthesized in a one-pot manner by subsequently adding BF_3•OEt_2 to the reaction mixture without isolating aza-dipyrrin intermediates (Scheme 3). Thanks to the broad scope of lactam structures for this Schiff base forming reaction, we and other groups have successfully converted a variety of lactams, such as benzo[*c*,*d*]indole,[23] diketopyrrolopyrrole (DPP),[24] isoindigo, benzodipyrrolidone[25] and N-confused oxoporphyrin,[26] into the corresponding aza-BODIPY analogues. In this Feature Article, the synthesis and structural features of these aza-BODIPY compounds as well as their unique optical properties, which are featured by NIR fluorescence, solid-state emission and aggregation-induced emission enhancement (AIEE), are introduced together with recent examples of BODIPY analogues with similar structures and NIR fluorescent properties as a comparison. In addition, application studies, such as organic photovoltaics, two-photon fluorescent probe, photoacoustic imaging and photothermal cancer therapy, are also summarized.

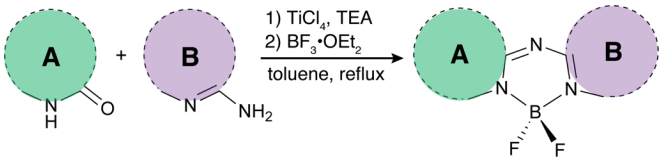

Scheme 3. aza-BODIPY synthesis based on a Schiff base forming reaction. A and B represent heteroaromatic rings.

2. Synthesis and optical properties of monomeric aza-BODIPY analogues

2.1 Benzo[*c*,*d*]indole-containing aza-BODIPY

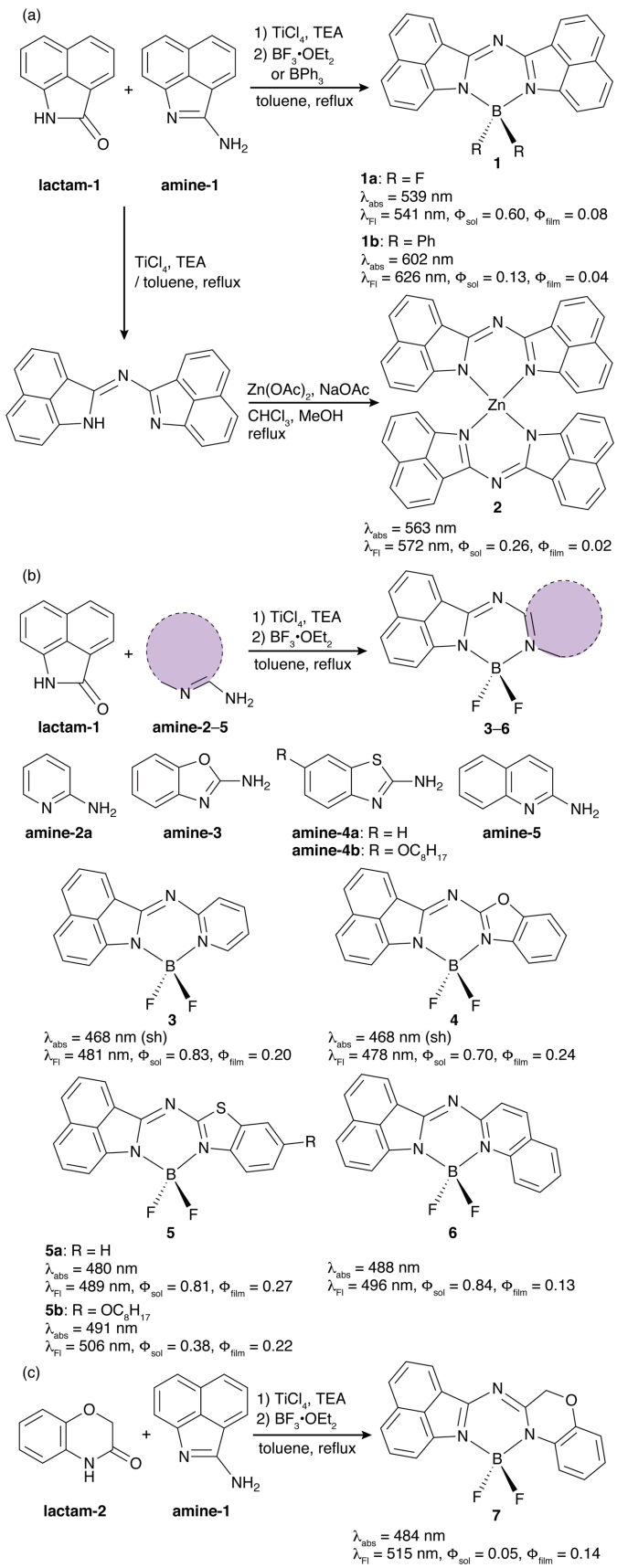

Scheme 4. Synthesis of (a) symmetric and (b, c) asymmetric benzo[*c*,*d*]indole-containing aza-BODIPY analogues. λ_{abs} and λ_{fl} are absorption and fluorescence maxima in $CHCl_3$ solution. Φ_{sol} and Φ_{film} denote fluorescence quantum yields in $CHCl_3$ solution and in a drop film state.

Monomeric aza-BODIPYs[23] were synthesized by the Schiff base forming reaction, which was developed for the first time by us to synthesize dimeric aza-BODIPY analogues from DPP.[24] For this synthesis, commercially available benzo[*c*,*d*]indole-2(1*H*)-one was utilized as a lactam structure.

A symmetric benzo[*c*,*d*]indole-containing aza-BODIPY **1**[27] was synthesized from benzo[*c*,*d*]indole-2(1*H*)-one (**lactam-1**) and benzo[*c*,*d*]indole-2-amine (**amine-1**), which was derived in four steps from **lactam-1** (Scheme 4a).[23] Its aza-dipyrrin ligand structure can be isolated without addition of boron reagents and converted into a dimeric zinc complex **2**. Broad substrate scopes of not only heteroaromatic amines (**amine-2**–**5**), but also lactam (**lactam-2**) for this Schiff base forming reaction have been disclosed (Scheme 4b and 4c). A similar series of benzo[*c*,*d*]indole-containing aza-BODIPY analogues were also independently reported by Jiao and Ran et al.[28]

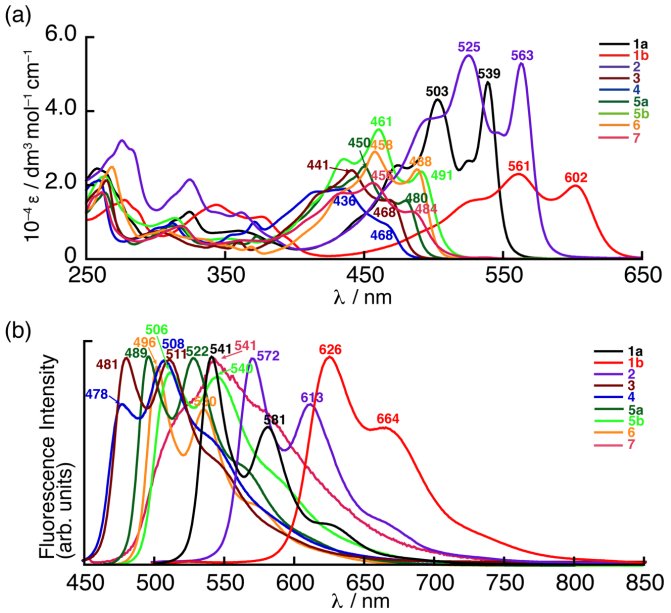

Fig. 3. (a) UV/vis absorption and (b) fluorescence spectra of benzo[*c*,*d*]indole-containing aza-BODIPY analogues in $CHCl_3$. Redrawn with permission from ref. 23 Copyright 2015 Wiley-VCH.

All the benzo[*c*,*d*]indole-containing aza-BODIPY analogues exhibited main absorption in the visible region from 400 to 600 nm (Fig. 3a). The absorption spectra of symmetric type compounds (**1** and **2**) were featured by two intense bands in longer wavelength region compared to those of asymmetric type compounds (**3**–**7**), which showed a broad band with a lower-energy shoulder. Contrary to the general trend of red-shifts from BODIPY to aza-BODIPY, the main absorption band of **1** rather shifted to the blue from that of its *meso*-carbon counterpart (**8**) at 622 nm.[29] To give the insight into this blue-shift, density functional (DFT) calculations were carried out. In the frontier MO diagrams, the HOMO is significantly stabilized (Fig. 4). This is in contrast to the conventional BODIPY–aza-BODIPY relationship, which shows stabilization of the LUMO (Fig. 2). This opposite relationship can be explained in terms of MO distribution patterns of the HOMO and LUMO. The HOMO of **1** is localized on the *meso*-position, whereas a node can be found at the same position in the LUMO. The nitrogen substitution

thus stabilized the HOMO rather than the LUMO, which causes increase of the ΔHL from **8** to **1**.

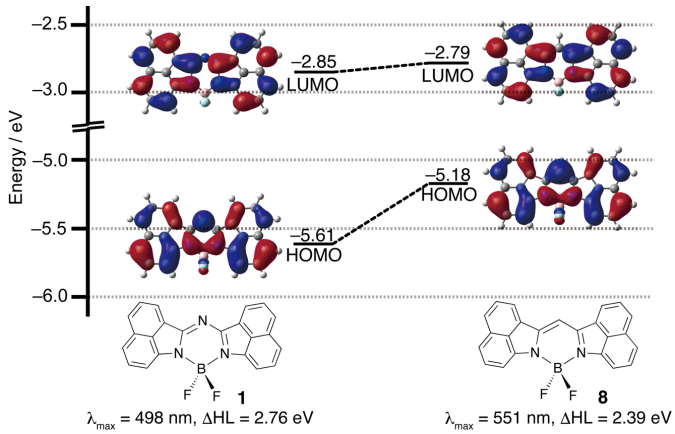

Fig. 4. Frontier MO diagrams and the lowest transition energies (λ_{max}) of **1** and **8** (B3LYP/6-31G(d)). Redrawn with permission from ref. 23 Copyright 2015 Wiley-VCH.

Jiao and Ran synthesized benzo[*c*,*d*]-containing BODIPY analogues, *meso*-carbon-substituted counterparts of **3**, **5** and **6**, and observed similar blue-shifts of absorption from the BODIPY structures to the corresponding aza-BODIPY structures. This opposite BODIPY–aza-BODIPY relationship in the absorption spectra can thus be regarded as a general trend of benzo[*c*,*d*]-containing aza-BODIPY compounds.

The fluorescence spectra of these series of benzo[*c*,*d*]indole-containing aza-BODIPY analogues were observed in the visible region with Stokes shifts of 69–1244 cm^{-1} and intense vibronic 0–1 bands (Fig. 3b). Considering the absorption and fluorescence spectral profiles and their overlaps, the lower-energy shoulders and the main band observed for the asymmetric type compounds (**3**–**7**) can be assigned to the 0–0 band and vibronic 0–1 band, respectively (Fig. 5). Despite the small Stokes shifts, except for **5b** and **7**, their fluorescence quantum yields were as high as 0.60–0.83. This can be ascribed to rather small overlaps of absorption and fluorescence spectra caused by the contribution of the vibronic bands. **7** was found to be less fluorescent because of the nonradiative decay processes caused by the structural flexibility around the sp^3 carbon moiety.

In the solid state, three types of changes of fluorescent properties from those in solution were observed (Fig. 6). The fluorescence of the symmetric type compounds (**1** and **2**) was nearly quenched, and the fluorescence quantum yields dropped to 0.02–0.08. This type of aggregation-caused quenching (ACQ) is normally observed for fluorescent compounds with small Stokes shifts. In contrast, the asymmetric type compounds (**3**–**6**) exhibited moderately high fluorescence quantum yields of 0.13–0.27 despite the similarly small Stokes shifts. In the case of **7**, the fluorescence quantum yield in the solid state is rather higher than that in solution, which can be regarded as an aggregation-induced emission enhancement (AIEE)[30] behaviour. In general, solid-state fluorescent compounds share some features such as large Stokes shifts in solution[31] and bulky

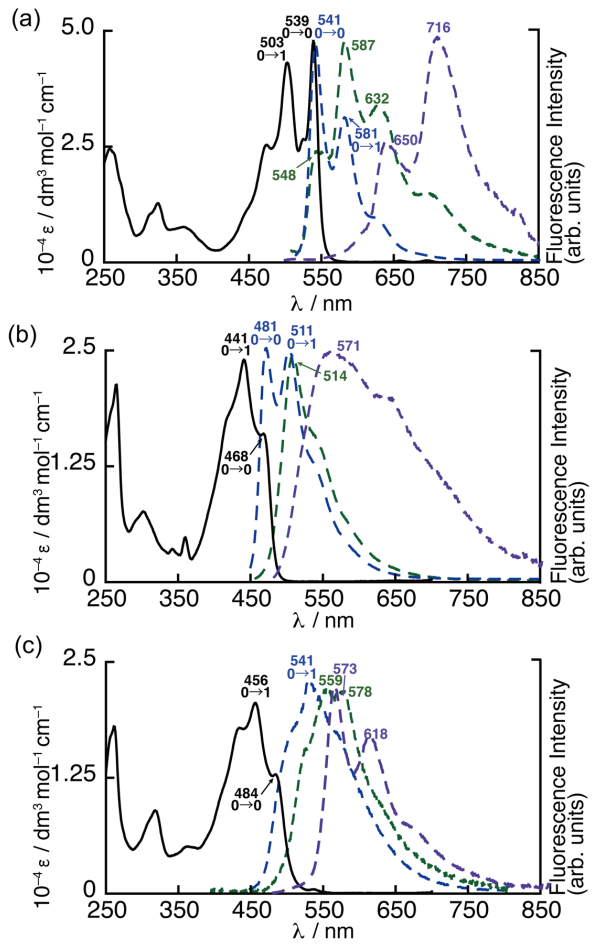

Fig. 5. UV/vis absorption in $CHCl_3$ (black solid line) and fluorescence spectra of (a) **1a**, (b) **3** and (c) **7** in $CHCl_3$ solution (blue dashed line), a PMMA film (green dashed line) and drop-cast film (violet dashed line). Redrawn with permission from ref. 23 Copyright 2015 Wiley-VCH.

substituent in the structure, which can minimize interchromophore interaction in the solid state. Neither is the case for these asymmetric type compounds. Two factors can be considered to explain the observed moderate solid-state emission of compounds **3**–**6**, instead. The one is the small overlap of the absorption and fluorescence spectra caused by the weak 0–0 absorption band and the intense 0–1 vibronic band in solution, which can reduce self-absorption in the solid state. In poly(methyl methacrylate) (PMMA) films, which exhibited similar absorption spectra to those in solution, the 0–0 emission band became weaken or disappeared. Owing to the intense 0–1 emission band in the PMMA film state, the asymmetric type compounds exhibited fluorescence quantum yields as high as those in solution (Fig. 6). The other factor is deviations of the directions of transition dipole moments between the nearest neighbour in the solid state, which may reduce cancellation of dipole moments, so that the emission was not completely quenched. Recently, Würthner et al. reported the detail about this kind of solid-state emission mechanism in the case ofity

their merocyanine dyes.[32]

In addition to the moderate ACQ effect due to the asymmetric structure, restricted structural dynamics around

the sp^3 carbon moiety of **7** induce the AIEE behaviour in the solid state. The AIEE behaviour is more significant in a poor solvent. When a water fraction in THF solution of **7** was increased, a significant jump of the fluorescence quantum yield was observed (Fig. 7). This is a typical AIEE response, and to the best of our knowledge, **7** is the first aza-BODIPY analogue exhibiting an AIEE behaviour.

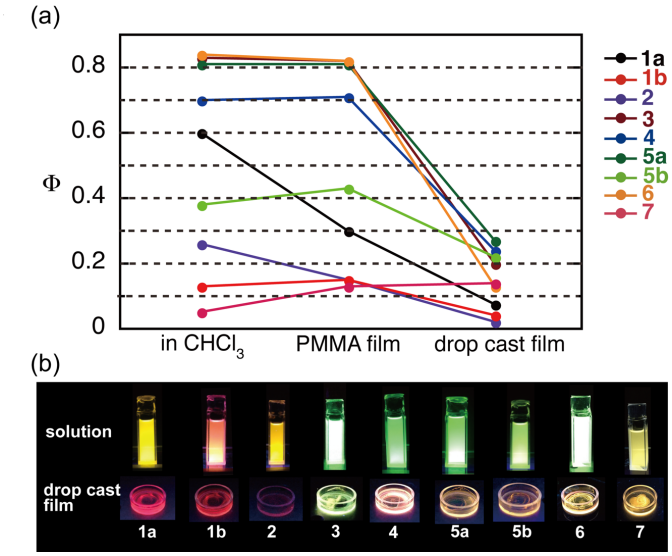

Fig. 6. (a) Plots of fluorescence quantum yields of a chloroform solution (left), a PMMA film (middle) and a drop cast film (right). (b) Photographs of a chloroform solution (top) and drop cast film (bottom) under irradiation by 365 nm lamp. Redrawn with permission from ref. 23 Copyright 2015 Wiley-VCH.

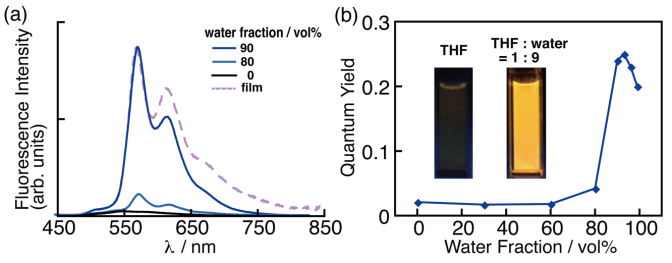

Fig. 7. (a) Changes of fluorescence spectra of **7** upon increasing a water fraction of THF/water mixture. The fluorescence spectrum of a drop-cast film of **7** is shown as a reference. (b) Dependence of fluorescence quantum yields of **7** on water fractions. Inset: Photographs of solutions under irradiation by 365 nm lamp. Redrawn with permission from ref. 23 Copyright 2015 Wiley-VCH.

2.2 aza-BODIPYs from keto-imine derivatives

Recently, Hua et al. revealed that the Schiff base forming reaction strategy towards the synthesis of aza-BODIPY analogues can also be applied to aromatic compounds bearing a keto-imine moiety, such as 3-iminoisoindolin-1-one[33] and 3-imino-2,3-dihydro-1*H*-benzo[*de*]isoquinolin-1-one.[34] From a simple refluxing of keto-imine precursors and heteroaromatic amines in ethanol, aza-dipyrrin structures were formed in high yields. The aza-dipyrrin ligands were subsequently converted into the corresponding aza-BODIPY structures upon treatment with BF_3•OEt_2 in the presence of TEA (Scheme 5).

Both isoindole-containing aza-BODIPY analogues (**9**–**12**) and azaphenalene-containing aza-BODIPY analogues (**13**–**15**) exhibited intense absorption and fluorescence in the visible region at around 380–430 nm and 400–550 nm, respectively. While vibronic bands can be clearly observed for **9**–**12** probably due to the rigid structures, the absorption and fluorescence spectra of **13**–**15** was rather structureless (Figs. 8 and 9). The relative intensities of the 0–0 band and 0–1 band of

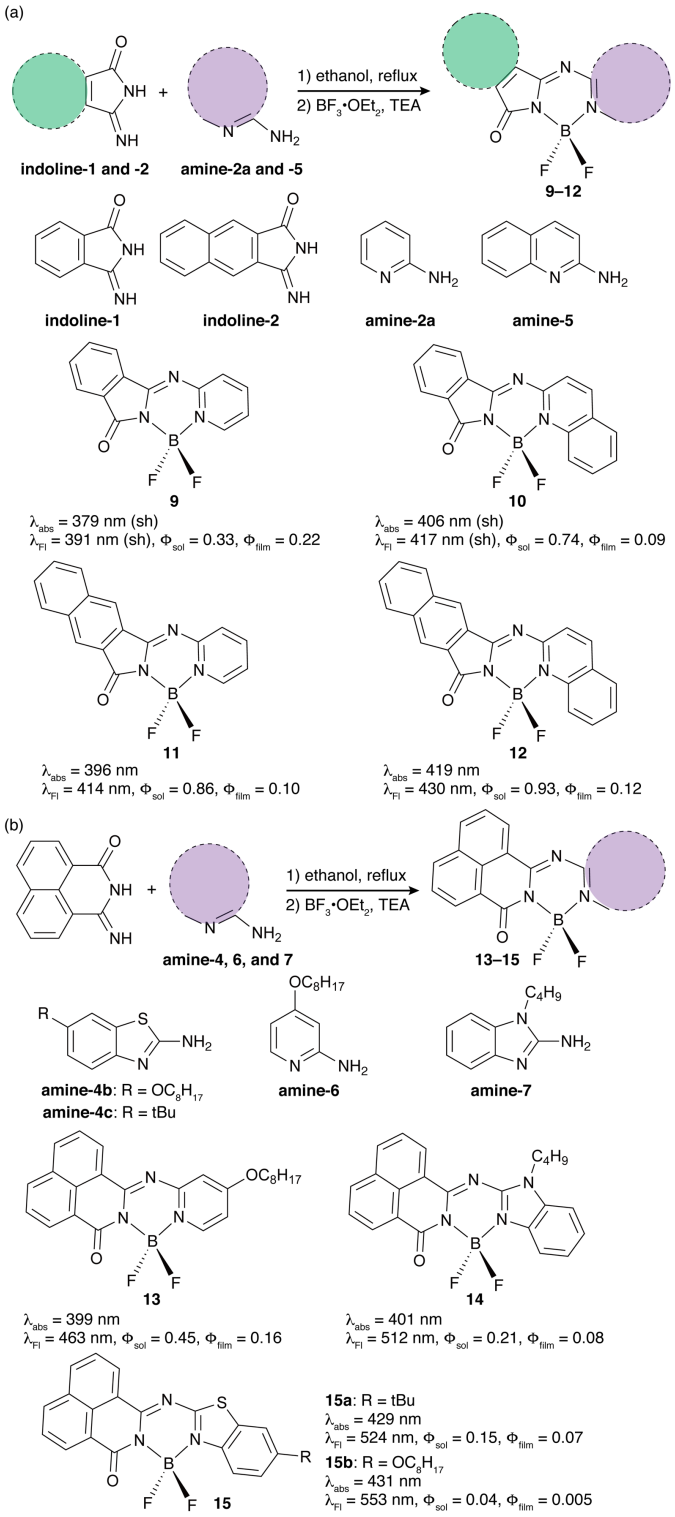

Scheme 5. Synthesis of (a) isoindole-containing aza-BODIPY analogues **9**–**12** and (b) azaphenalene-containing aza-BODIPY analogues **13**–**15**. λ_{abs} and λ_{fl} are absorption and fluorescence maxima in CH_2Cl_2 solution. Φ_{sol} and Φ_{film} denote fluorescence quantum yields in CH_2Cl_2 solution and in a drop film state.

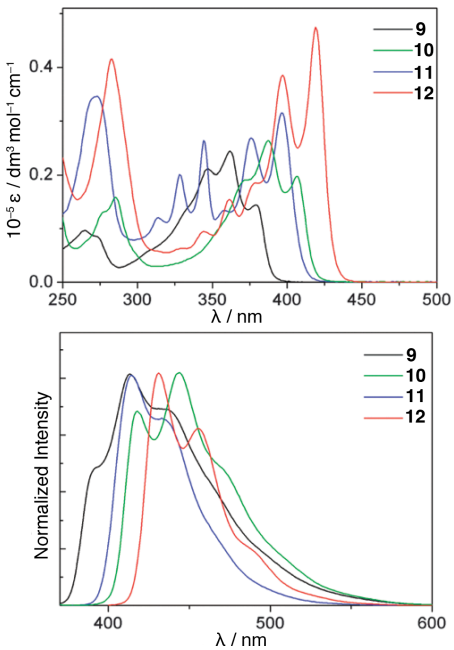

Fig. 8. UV/vis absorption (top) and fluorescence (bottom) spectra of isoindole-containing aza-BODIPY analogues **9**–**12** in CH_2Cl_2. Redrawn with permission from ref. 33 Copyright 2014 RSC.

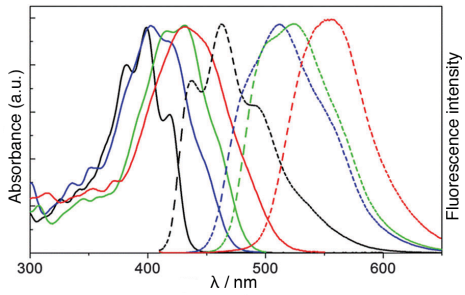

Fig. 9. UV/vis absorption (solid lines) and fluorescence (dashed lines) spectra of azaphenalene-containing aza-BODIPY analogues **13** (black lines), **14** (blue lines), **15a** (green lines) and **15b** (red lines) in CH_2Cl_2. Redrawn with permission from ref. 34 Copyright 2015 RSC.

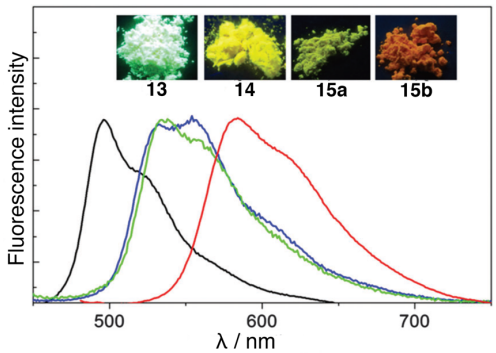

Fig. 10. Emission spectra of azaphenalene-containing aza-BODIPY analogues **13** (black line), **14** (blue line), **15a** (green line) and **15b** (red line) in powder. Inset: photographs of powders of **13**–**15** under irradiation by 365 nm lamp. Redrawn with permission from ref. 34 Copyright 2015 RSC.

isoindole-containing compounds **9**–**12** were largely affected by benzo-annulation at the isoindoline moiety from **9** to **11** and from **10** to **12**. In addition to the intense fluorescence in solution, these aza-BODIPY analogues bearing a keto moiety exhibited moderate solid-state emission, which can be ascribed to their asymmetric structures as with the asymmetric types of benzo[*c*,*d*]indole-containing aza-BODIPY analogues (Fig. 10).[23]

3. Synthesis and optical and electrochemical properties of dimeric aza-BODIPY analogues

Recently, a variety of bis-lactam compounds have been synthesized owing to their application as an acceptor unit in low band gap donor-acceptor small molecules and polymers in organic electronics.[35–37] Among bis-lactam compounds, diketopyrrolopyrrole (DPP),[24] benzodipyrrolidone and isoindigo[25] were selected to synthesize dimeric aza-BODIPY analogues using the Schiff base forming reaction.

3.1 Pyrrolopyrrole aza-BODIPY analogues

DPP has been frequently utilized as a red pigment in industry.[38] In recent years, DPP-based donor-acceptor small molecules and polymers have been investigated as functional materials for organic electronics due to the excellent photophysical properties such as robustness and intense absorption at around 500 nm in the visible region.[39,40] We expected that elongation of the conjugated systems through the carbonyl moieties using our Schiff base forming reaction strategy causes red-shifts of both absorption and emission of DPP. Although there have been several reports on the structural modification of DPP at the pyrrolic nitrogen atom and aryl substituents,[41] such modification has been limited due to the inherently low reactivity of the carbonyl moieties of DPP.[42]

Zumbusch and Daltrozzo pioneered functionalization of the carbonyl moieties of DPP and synthesized cyanine dyes comprising a pyrrolopyrrole moiety called as pyrrolopyrrole cyanines (PPCys) from DPP and heteroarylacetonitriles (**acetonitrile-1–6**) in the presence $POCl_3$ (Scheme 6).[43] PPCys exhibited intense absorption and emission in the far-red and NIR regions as shown in Fig. 11. Owing to the broad scope of heteroarylacetonitriles in the synthesis of PPCys, a series of PPCy molecules bearing a variety of heteroaromatic ring units have been reported.[44] In Scheme 6, some representative structures (**16**–**21**) are listed. They have extended their study to applications, such as NIR fluorescence probe[45] and photoacoustic imaging.[46]

Considering the BODIPY–aza-BODIPY relationship, we attempted to synthesize aza-BODIPY analogues of PPCy, which we referred to as pyrrolopyrrole aza-BODIPY (PPAB) with the aim of shifting absorption and emission further to the red. The first-generation PPABs was thus synthesized by the $TiCl_4$-mediated Schiff base forming reaction of DPP and heteroaromatic amines and subsequent BF_2 complexation (Scheme 7). These PPABs exhibited intense absorption at around 650 nm and a mirror-imaged fluorescence in the far-red region with high fluorescence quantum yields of Φ = 0.81–0.87 (Fig. 12). Upon expansion of the heteroaromatic ring units from **22** to **24**, the absorption and emission became gradually red-shifted (**22a**: λ_{abs} = 638 nm, λ_{Fl} = 661 nm, **23a**: λ_{abs} = 655 nm, λ_{Fl} = 676 nm, **24**: λ_{abs} = 671 nm, λ_{Fl} = 692 nm). In contrast to the moderate solid-state emission of benzo[*c*,*d*]indole-containing aza-BODIPY, the fluorescence of PPABs was virtually quenched in the solid state.

On one hand, compared to DPP, which shows a similarly intense absorption at around 500 nm, the absorption bands of

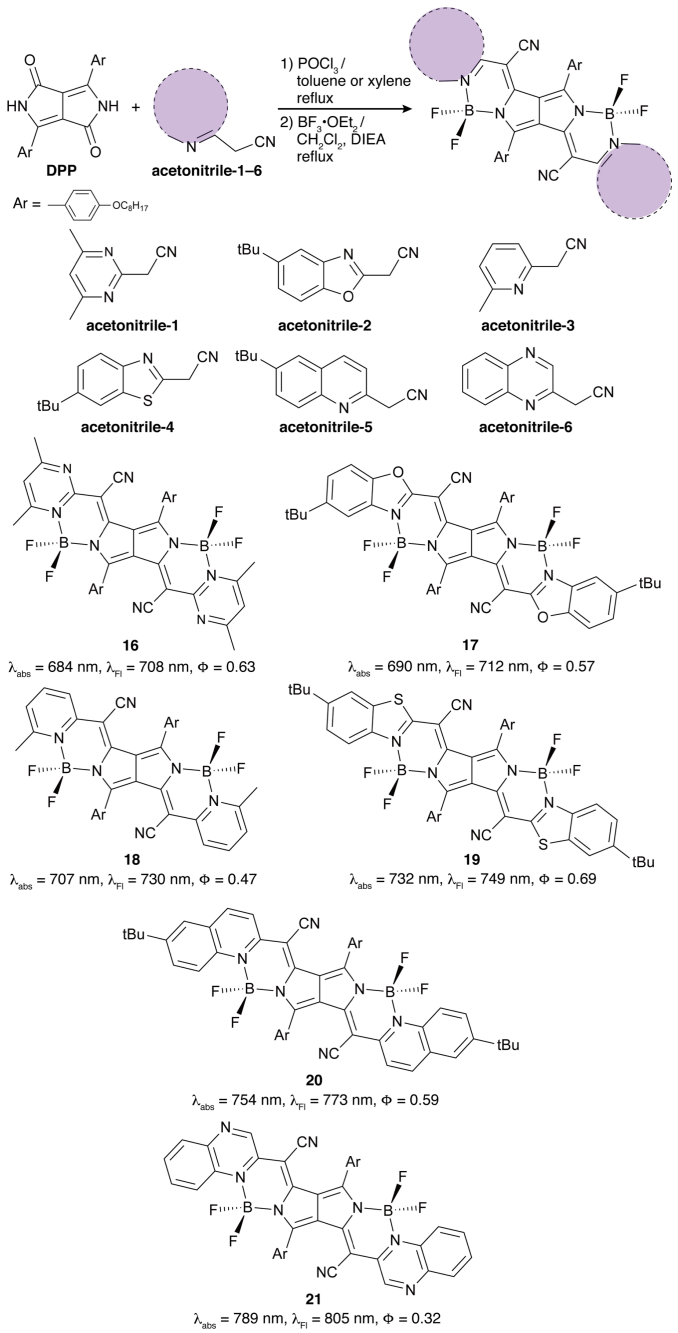

Scheme 6. Synthesis of PPCys **16**–**21**. λ_{abs} and λ_{fl} are absorption and fluorescence maxima in $CHCl_3$ solution. Φ denotes fluorescence quantum yields in $CHCl_3$ solution.

PPABs are bathochromically shifted as we expected. On the other hand, they are hypsochromically shifted from those of the corresponding PPCys. These blue-shifts of the main bands can be explained in terms of the MO distribution patterns of the HOMO and LUMO as with the relationship observed for benzo[*c*,*d*]indole-containing BODIPY and aza-BODIPY. Fig. 13 shows the frontier MO diagrams of **22** and the corresponding PPCy model structure (**25**). The HOMO and LUMO are delocalized on the entire molecule in both cases. The electron withdrawing cyano groups at the *meso*-positions stabilized the HOMO and LUMO, but the extent of stabilization of the LUMO (0.21 eV) is more significant than that of the HOMO (0.06 eV).

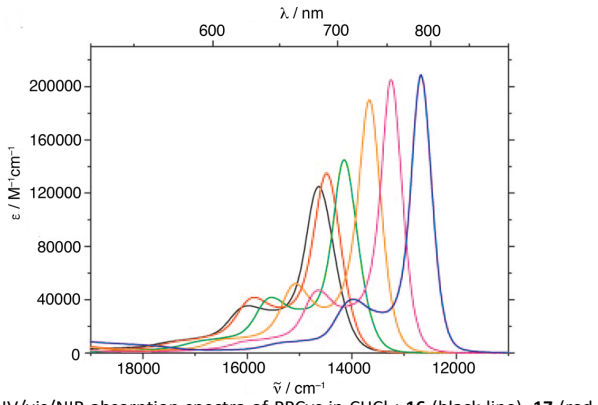

Fig. 11. UV/vis/NIR absorption spectra of PPCys in $CHCl_3$: **16** (black line), **17** (red line), **18** (green line), **19** (orange line), **20** (magenta line) and **21** (blue line). Redrawn with permission from ref. 43b Copyright 2009 Wiley.

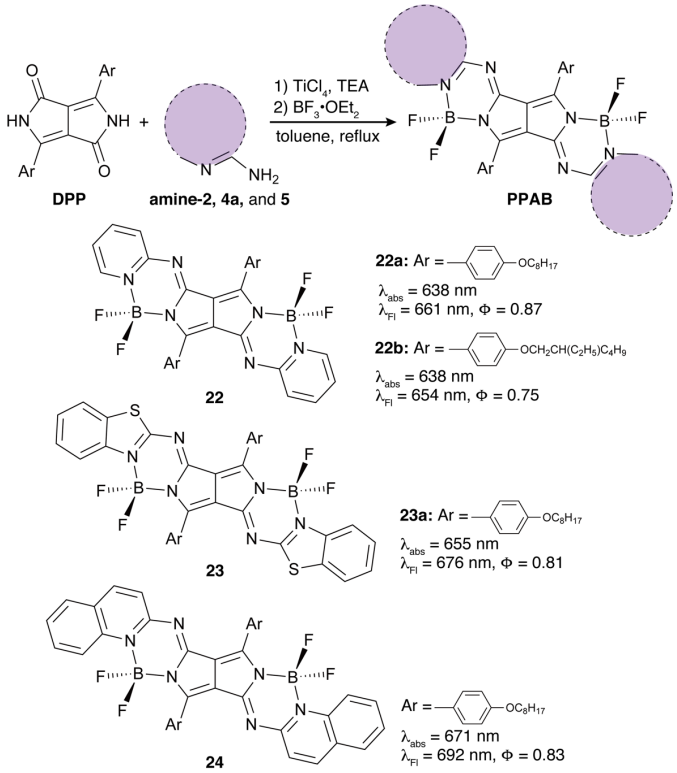

Scheme 7. Synthesis of the first-generation PPABs. λ_{abs} and λ_{fl} are absorption and fluorescence maxima in $CHCl_3$ solution. Φ denotes fluorescence quantum yields in $CHCl_3$ solution.

Therefore, the ΔHL of PPCys becomes narrower compared to that of PPABs.

Despite the blue-shift of the absorption and fluorescence of PPABs from those of the corresponding PPCys, we expected that effects of the aryl substituents at the DPP moiety on the optical properties were more significant because of the smaller dihedral angles between the substituents and the core structure (PPCy **20**: 64˚ and PPAB **24**: 30˚ as shown in Fig. 14). Considering less steric hindrance around the *meso*-positions of PPABs compared to PPCys bearing cyano group at the *meso*-positions, introduction of substituents at the aryl positions can be regarded as an efficient method to shift the absorption and emission of PPAB into the NIR region in addition to modification of the heteroaromatic ring unit to larger ring systems.

Based on these ideas, we took three PPAB structures (**M-1**–**3**) into consideration, and the lowest transition energies and the frontier MO diagrams were compared with those of **23** (Fig. 15).[47] **M-1** comprises polycyclic benzo[*c*,*d*]indole, whereas **M-2** and **M-3** possess electron-donating *N*,*N*-dimethylaminophenyl substituents and thienyl substituents, respectively. In the case of **M-3**, less steric congestion around the thienyl substituent than phenyl substituents allows **M-3** to take much smaller dihedral angles, which may enhance substituent perturbation.

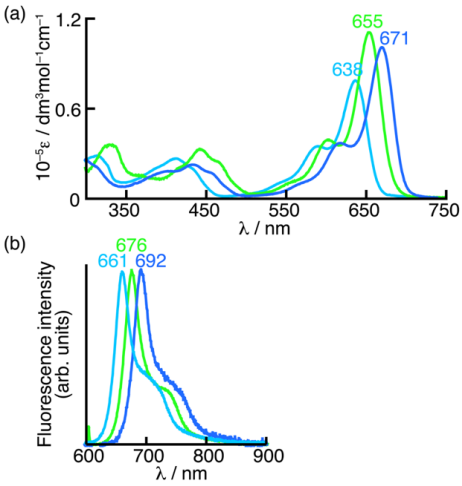

Fig. 12. (a) UV/vis absorption and (b) fluorescence spectra of **22a** (aqua blue), **23a** (green) and **24** (blue) in $CHCl_3$. Redrawn with permission from ref. 24 Copyright 2013 RSC.

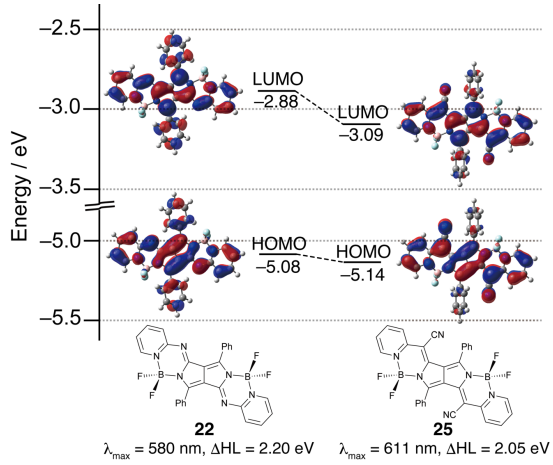

Fig. 13. Frontier MO diagrams and the lowest transition energies (λ_{max}) of representative PPAB **22** and the corresponding PPCy model structure (**25**) (B3LYP/6-31G(d)).

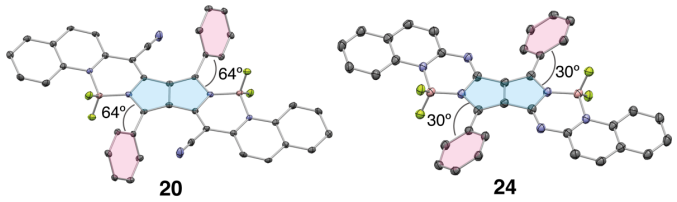

Fig. 14. X-ray single crystal structures of PPCy **20** and PPAB **24** and comparison of the dihedral angles between the aryl substituents (pink) and the core structure (aqua blue). Hydrogen atoms and alkyl and alkoxy substituents are omitted for clarity.

As we expected, these modifications were found to be effective. Narrower ⊿HL and red-shifts of the lowest absorption bands were predicted by the TDDFT calculations (**23**: ⊿HL = 2.16 eV, λ_{max} = 600 nm, **M-1**: ⊿HL = 1.88 eV, λ_{max} = 689 nm, **M-2**: ⊿HL = 1.94 eV, λ_{max} = 666 nm, **M-3**: ⊿HL = 2.03 eV, λ_{max} = 628 nm).

Based on these theoretical predictions, the second-generation PPABs **26**–**31** were synthesized by the Schiff base forming reaction of the corresponding DPPs and heteroaromatic amines (Fig. 16). In the case of thienyl-substituted PPAB **28**, the thienyl substituents were further extended to bithienyl (**30**) and terthienyl (**31**) by bromination of the terminal positions (**29**) and following Suzuki-Miyaura coupling reactions (Scheme 8).

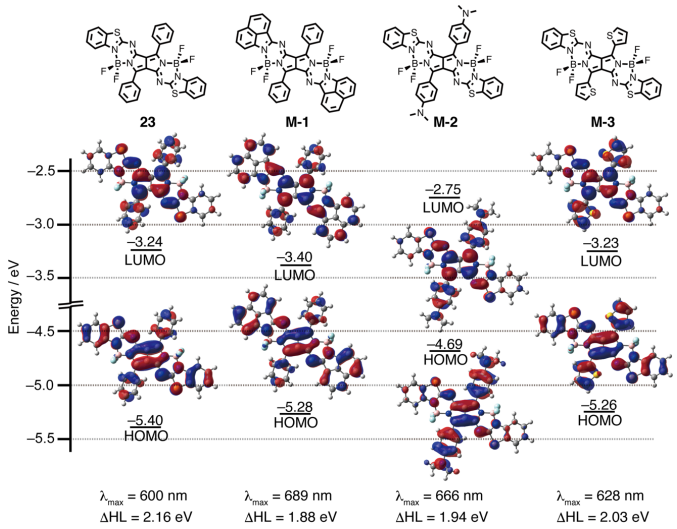

Fig. 15. Frontier MO diagrams and the lowest transition energies (λ_{max}) of PPAB model structures **M-1**–**3** and a reference structure **23** (B3LYP/6-31G(d)). Redrawn with permission from ref. 47 Copyright 2015 Wiley.

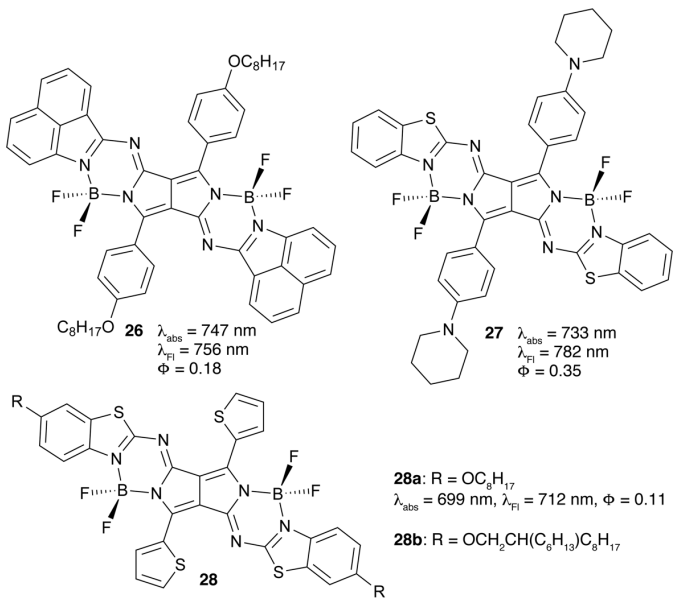

Fig. 16. Structures of the second-generation PPABs. λ_{abs} and λ_{fl} are absorption and fluorescence maxima in $CHCl_3$ solution. Φ denotes fluorescence quantum yields in $CHCl_3$ solution.

All of the second-generation PPABs exhibited absorption and fluorescence in the longer wavelength region compared with those of the first-generation PPABs, **22**–**24** (Fig. 17a). A sizable red- shift of absorption by 92 nm from that **23a** was

observed for **26** bearing benzo[*c*,*d*]indole moieties as a heteroaromatic ring unit. Piperidinophenyl (**27**) and thienyl (**28**) substituents also caused red-shifts by 78 nm and 44 nm from **23a**, respectively. Due to the donor-acceptor nature, the main absorption band of **27** became broad and less intensified along with appearance of a new band at around 500 nm, which can be assigned as an intramolecular charge-transfer band. The red-shift from **23a** to **28** can be ascribed to the small dihedral angle of the thienyl substituents (27˚) as well as their electron-donating nature.[48] Gradual red-shift from **28** by about 50 nm per thiophene unit was observed upon extension of the thienyl substituents to bithienyl (**30**: 756 nm) and terthienyl (**31**: 803 nm) substituents.

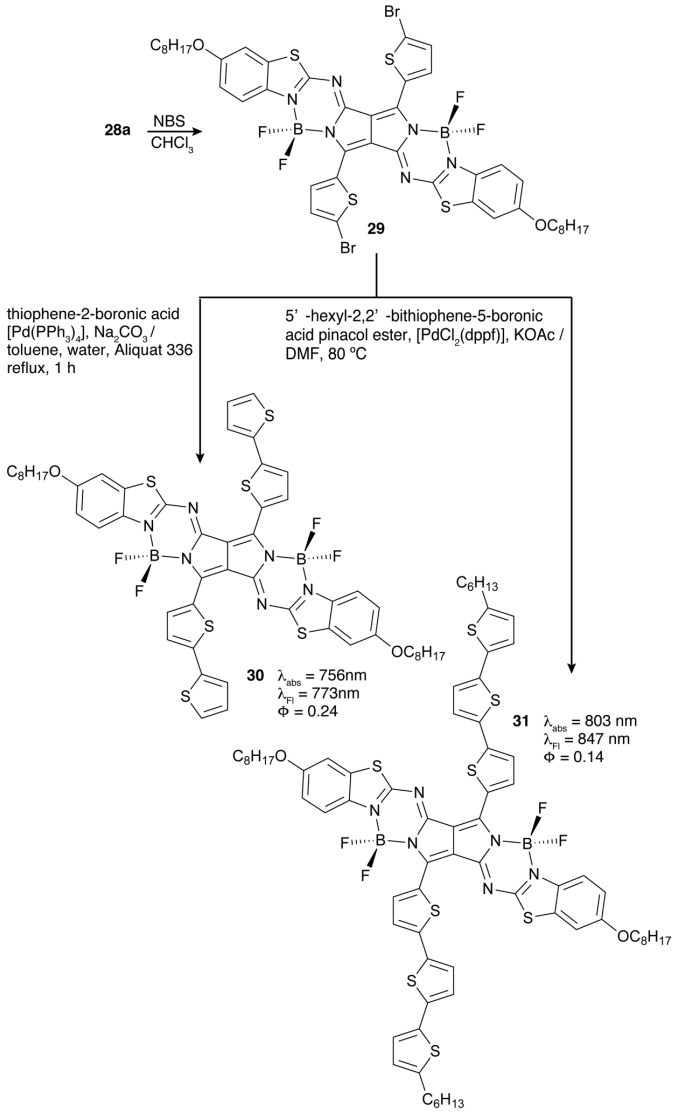

Scheme 8. Synthesis of the second-generation PPABs by Suzuki-Miyaura coupling reactions. λ_{abs} and λ_{fl} are absorption and fluorescence maxima in $CHCl_3$ solution. Φ denotes fluorescence quantum yields in $CHCl_3$ solution.

The fluorescence spectra of the second-generation PPABs also shifted to the red in the same order as observed for the absorption spectra (Fig. 17b). Except for **27** with piperidinophenyl groups and **31** with terthienyl groups, the Stokes shifts were modest (159–291 cm^{-1}) reflecting the rigid PPAB chromophore structure. Intramolecular charge-transfer nature and dynamics of the terthienyl groups can be ascribed to rather large Stokes shifts of **27** (855 cm^{-1}) and **31** (647 cm^{-1}). The fluorescence quantum yields were relatively high as a fluorophore in the far-red and NIR regions (Φ = 0.11–0.35).

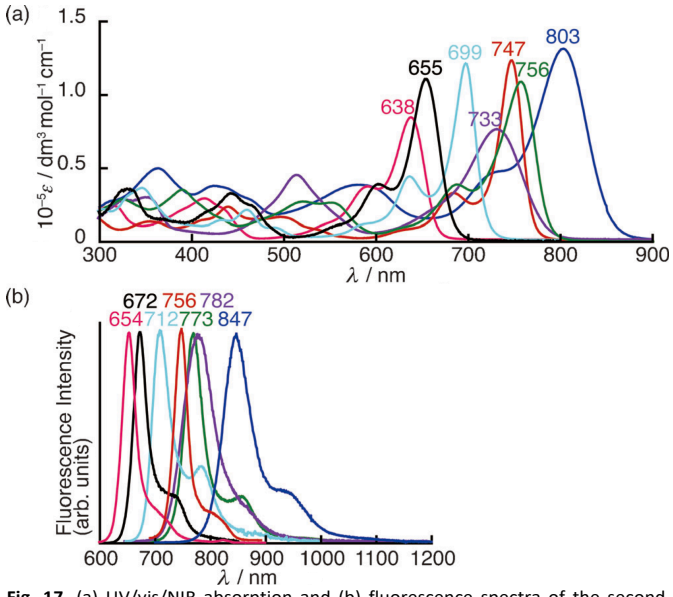

Fig. 17. (a) UV/vis/NIR absorption and (b) fluorescence spectra of the second-generation PPABs; **26** (red line), **27** (purple line), **28a** (aqua blue line), **30** (green line), and **31** (blue line) in $CHCl_3$. UV/vis absorption and fluorescence spectra of the first-generation PPABs; **22b** (pink line) and **23a** (black line) in $CHCl_3$ are shown as references. Redrawn with permission from ref. 47 Copyright 2015 Wiley.

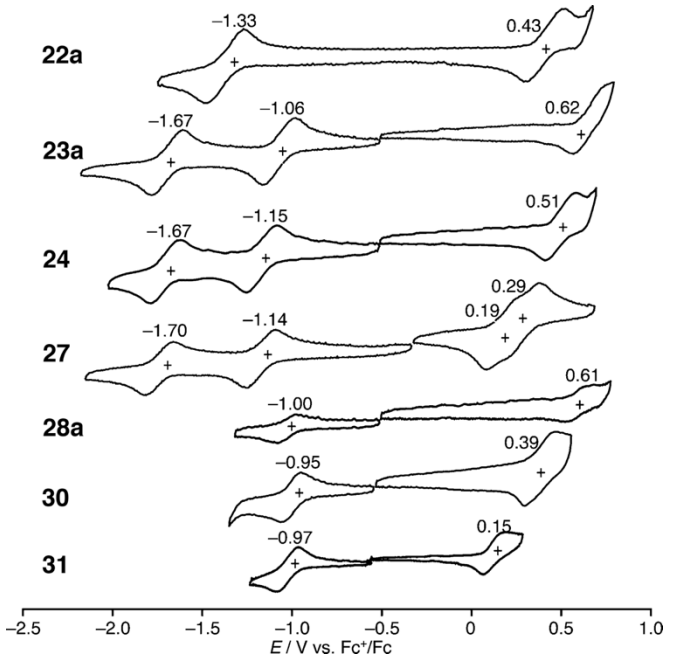

Fig. 18. Cyclic voltammograms of PPABs (0.5 mM) in *o*-dichlorobenzene containing 0.1 M tetra-*n*-butylammonium perchlorate as a supporting electrolyte at a scan rate of 100 mV s^{-1}. Values are half-wave potentials. Redrawn with permission from ref. 47 Copyright 2015 Wiley.

PPABs are electrochemically stable, exhibiting one or two reversible oxidation and reduction in the cyclic voltammetry measurements (Fig. 18). The following general trends of the potential shifts were observed by changing the heteroaromatic ring unit and introduction of electron-donating substituents. In

the case of substitution of the heteroaromatic unit from monocyclic pyridine (**22**) to bicyclic benzothiazole (**23**) and quinoline (**24**), the first reduction (**1stRed**; **22a**: –1.33 V vs. Fc^+/Fc, **23a**: –1.06 V, **24**: –1.15 V) shifted more positively compared to the first oxidation (**1stOx**; **22a**: 0.43 V, **23a**: 0.62 V, **24**: 0.51 V), which resulted in the narrower band gap (⊿HL). In contrast, the introduction of the electron-donating substituents caused negative shifts of **1stOx** (**27**: 0.19 V). In addition, gradual negative shifts of **1stOx** were observed by extension of the thienyl substituents (**30**: 0.39 V and **31**: 0.15 V). All of these shifts, which relate to the band gaps (⊿HL) of PPAB, are in good agreement with the observed red-shifts of the absorption spectra.

3.2 Benzodipyrrole and isoindigo aza-BODIPY analogues

Recently, Chen and our group independently reported the synthesis of dimeric aza-BODIPYs from benzodipyrrolidone[49] by the Schiff base forming reaction (Scheme 9).[25,50] We also revealed availability of isoindigo[51] for the aza-BODIPY synthesis. The single crystal X-ray diffraction analysis revealed a highly planar structure of benzodipyrrole aza-BODIPY (BDAB) **32** and a gable structure of isoindigo aza-BODIPY (IDAB) **33** with a highly twisted double bond by about 25˚ due to the steric hindrance between aza-BODIPY moieties (Fig. 19).

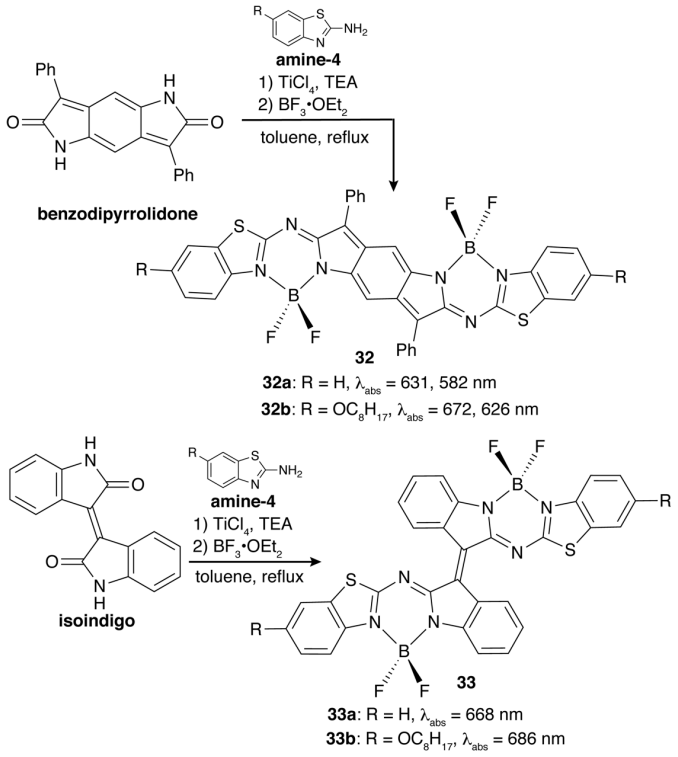

Scheme 9. Synthesis of BDAB **32** and IDAB **33**. λ_{abs} is absorption maxima in $CHCl_3$ solution.

Similar to the relationship between DPP and PPABs, upon converting the ketone moieties to aza-BODIPY structures, BDAB and IDAB exhibited the red-shifts of the main absorption from that of the corresponding benzodipyrrolidone (483 and 367 nm in *N*,*N*-dimethylformamide (DMF)) and isoindigo (453 nm in DMF) (Fig. 20). In contrast to the intense fluorescence property of PPABs, both BDAB and IDAB are virtually non-fluorescent.

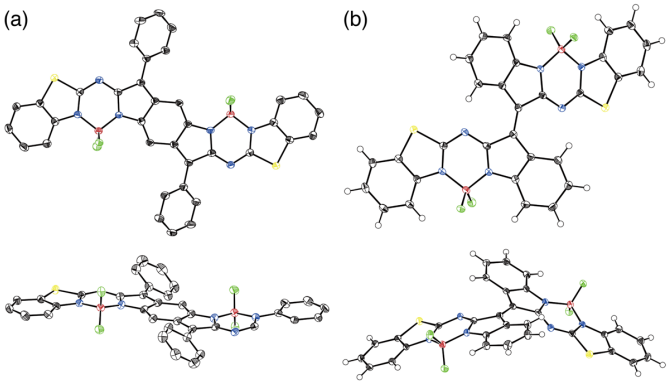

Fig. 19. X-ray single crystal structures of (a) **32b** and (b) **33a**, top views (top) and side views (bottom). The thermal ellipsoids are scaled to the 50% probability level. Hydrogen atoms and octyloxy substituents in panel a are omitted for clarity. Redrawn with permission from ref. 25 Copyright 2017 Elsevier.

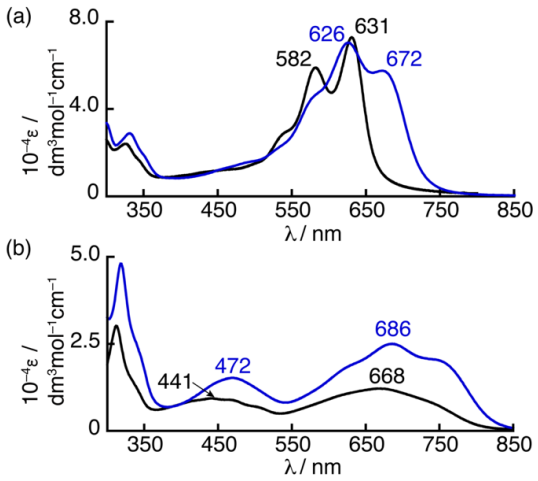

Fig. 20. UV/vis absorption spectra of (a) **32** (**32a**: black line and **32b**: blue line) and (b) **33** (**33a**: black line and **33b**: blue line) in $CHCl_3$. Redrawn with permission from ref. 25 Copyright 2017 Elsevier.

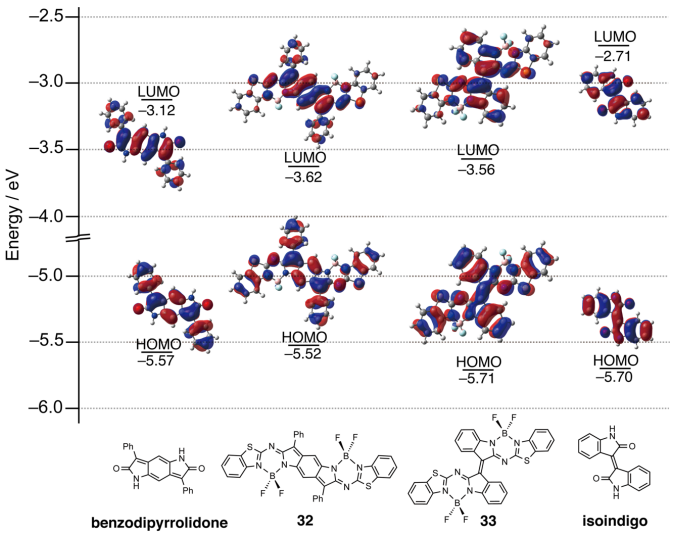

Fig. 21. Frontier MO diagrams of benzodipyrrolidone, isoindigo, **32** and **33** (B3LYP/6-31G(d)). Redrawn with permission from ref. 25 Copyright 2017 Elsevier.

Based on the TDDFT calculations, these red-shifts can be ascribed to significant stabilization of the LUMO compared to the HOMO (Fig. 21).

Chen et al. revealed the substituent effect on the red-shifts of the absorption spectra of BDAB **34** (Fig. 22).[50] The two main absorption of BDAB at around 550 nm, which was mentioned to be resembled to the absorption of bicyclo[2.2.2]octadiene-bridged bis-BODIPYs (504 and 544 nm),[52] shifted to the red with solution colour change from purple to sky blue by incorporation of electron-donating hexyloxy and/or 3-hexylthiophene-2-yl substituents. In contrast, there was minor effect of the weakly electron-withdrawing fluorine substituents.

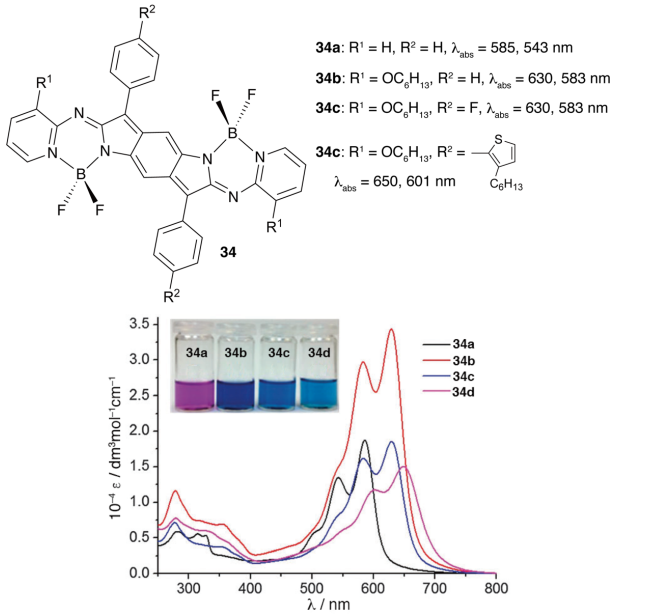

Fig. 22. Structures of substituted BDAB **34** (top) and their UV/vis absorption spectra (bottom) in CH_2Cl_2. λ_{abs} is absorption maxima in CH_2Cl_2 solution. Inset: A photograph of solution colours. Redrawn with permission from ref. 50 Copyright 2014 RSC.

BDAB and IDAB both exhibited two reversible reversible reduction waves at the half-wave potentials of –0.69 V and –0.87 V (vs. Fc^+/Fc) and –0.71 V and –0.90 V, respectively, whereas the oxidation process was irreversible (Fig. 23). Compared to the first reduction potentials of *N*,*N*′-dimethylbenzodipyrrolidone at –1.17 V[49] and *N*,*N*′-di-(1-octyl)-isoindigo at –1.34 V,[53] those of BDAB and IDAB shifted positively, which implies their electron-accepting natures.

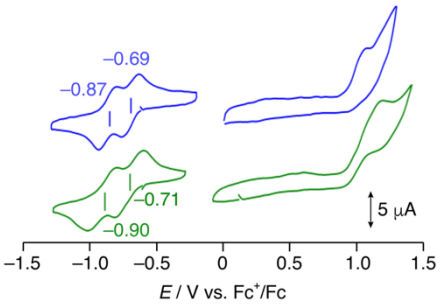

Fig. 23. Cyclic voltammograms of **32b** (blue line) and **33a** (green line) in *o*-dichlorobenzene containing 0.5 mM of sample and 0.1 M of tetra-*n*-butylammonium perchlorate as a supporting electrolyte. Scan rate: 100 mV s^{-1}. Values are half-wave potentials. Reprinted with permission from ref. 25 Copyright 2017 Elsevier.

3.3 PPAB dimers

Dimerization of chromophores is one of general strategies to drastically change their optical properties. In the research fields of BODIPY and aza-BODIPY analogues, various attempts have been devoted to create NIR chromophores and fluorophores. Representative example related to this Feature Article is a fused dimer of PPCy.[54] Fusion of BODIPY by sharing aromatic rings was reported to cause significant red-shifts of absorption and fluorescence.[52,55] Zumbusch et al. synthesized a benzo-bridged PPCy dimer (**36**) in a step-wise manner via a half-PPCy derivative (**35**) (Scheme 10). A striking feature of the UV/vis/NIR absorption of **36** is its transparency in the vis region and intense absorption above 700 nm (Fig. 24). Technical applications of such a unique chromophore have been of interest.

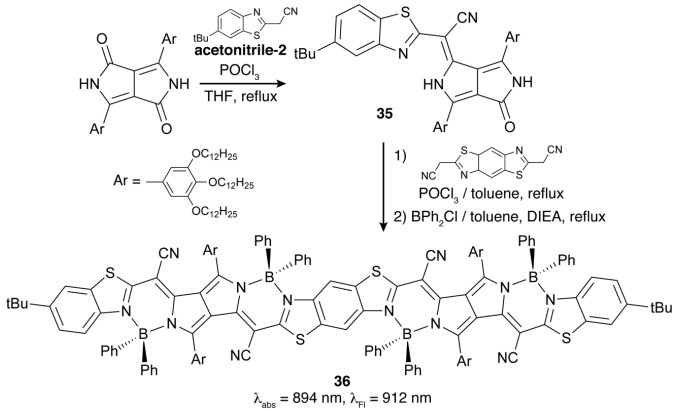

Scheme 10. Synthesis of benzo-bridged PPCy dimer (**36**). λ_{abs} and λ_{fl} are absorption and fluorescence maxima in $CHCl_3$ solution.

During the attempt to extend the thienyl substituents by Suzuki-Miyaura coupling reactions of brominated PPAB (**29**) via borylation reaction using a palladium catalyst, a bithienyl-linked dimer was formed as a homo-coupling product.[47] In contrast to the intense NIR absorption of the above-mentioned benzo-bridged PPCy dimer, this dimer exhibited panchromatic absorption in the vis/NIR regions. To give an insight into the role of the bridging unit, bithiophene-linked and biphenylene-linked dimers **38** and **40** were synthesized (Scheme 11), and the optical properties were compared.[56]

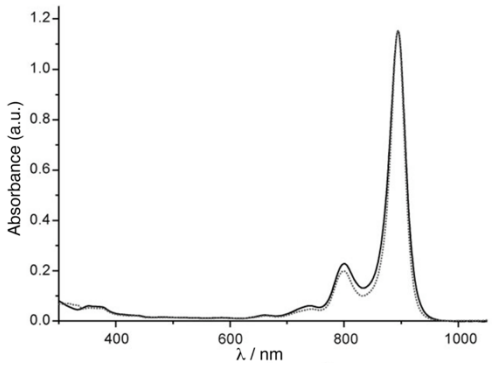

Fig. 24. UV/vis/NIR absorption spectra of **36** in $CHCl_3$ (dotted line) and in PMMA (solid line). Redrawn with permission from ref. 54 Copyright 2011 Wiley.

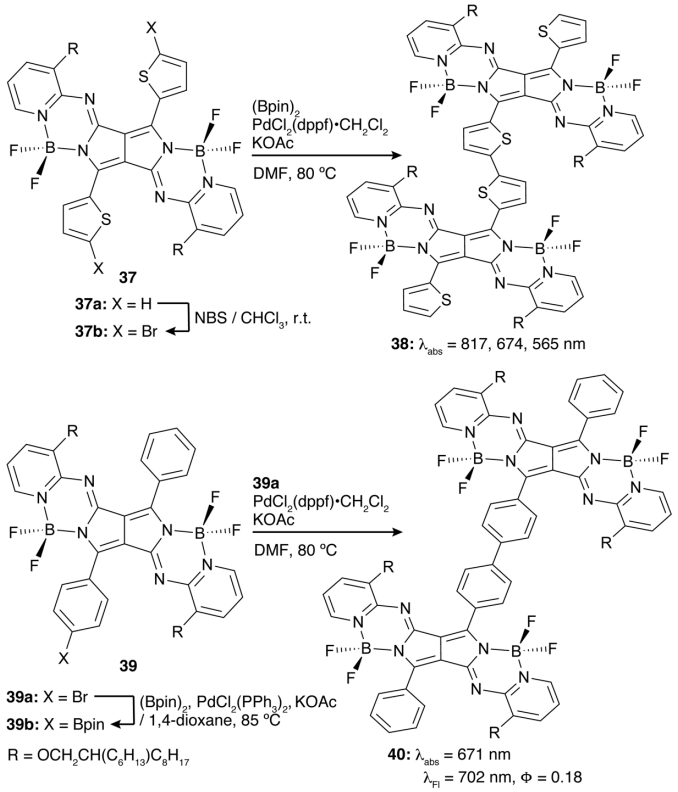

Scheme 11. Synthesis of PPAB dimers (**38** and **40**). λ_{abs} and λ_{fl} are absorption and fluorescence maxima in $CHCl_3$ solution. Φ denotes fluorescence quantum yields in $CHCl_3$ solution.

In clear contrast to the panchromatic absorption of bithienyl-linked PPAB dimer **38** in the vis/NIR regions, biphenyl-linked PPAB dimer **40** exhibited almost identical absorption spectral profile to that of the corresponding monomer species **41** with two-times larger molar absorption coefficients than that of **41** (Fig. 25). This result implies negligible chromophore–chromophore interactions through the biphenylene-linkage probably due to the twisted arrangement of the biphenylene and PPAB moieties.

In addition to the panchromatic absorption, bithienyl-linked PPAB **38** showed unique dual emission centred at 750 and 880 nm, the relative intensities of which were dependent on the excitation wavelengths (Fig. 26a). On the other hand, the fluorescence spectrum of the biphenylene-linked PPAB dimer **40** is independent from excitation wavelengths and similar to that of the corresponding monomer (Fig. 26c). Considering that similar dual emission properties of a butadiyne-linked porphyrin dimer[57,58] and a *meso*,*meso*-linked corrole dimer[59] were ascribed to rotational isomerism through the linkage unit, such dynamic behaviour of **38** was investigated by variable temperature ^{1}H NMR experiments and absorption and fluorescence spectroscopic measurements in a viscous solvent consisting of chloroform and paraffine oil (v/v = 1:2) (Fig. 26b and d).

In the viscous solution, contrary to the similar absorption spectrum of **38** to that in chloroform, the fluorescence spectrum exhibited a new emission band at 685 nm, which can be assigned to monomer-like emission due to rather slow rotation isomerism in the viscous solution.

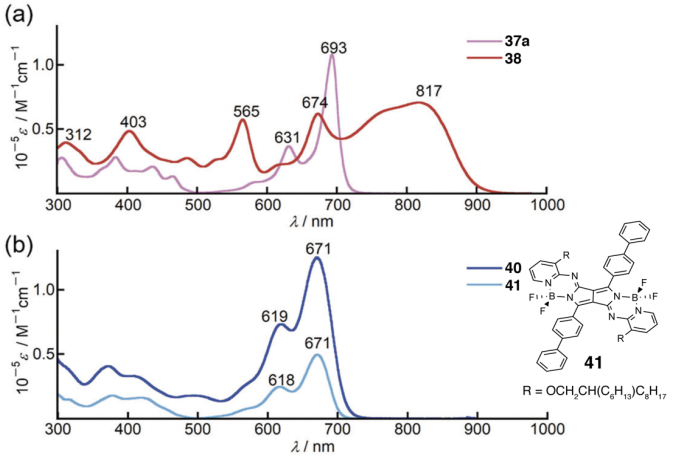

Fig. 25. UV/vis/NIR absorption spectra of (a) **37a** (pink line) and **38** (red line) and (b) **40** (blue line) and **41** (aqua blue line) in $CHCl_3$. Inset: structure of **41**. Redrawn with permission from ref. 56 Copyright 2018 RSC.

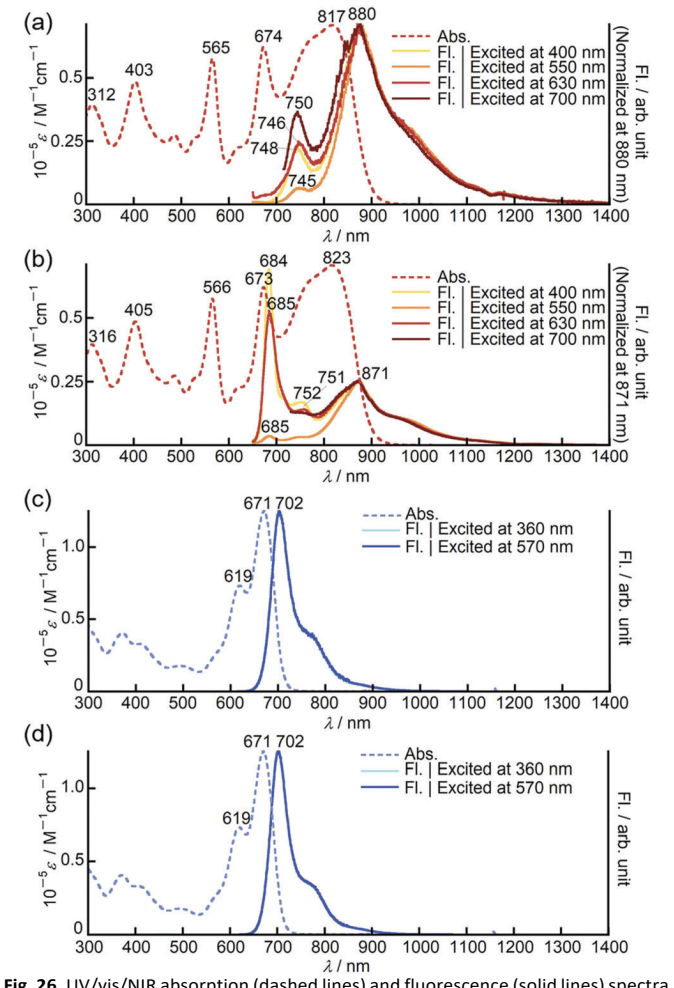

Fig. 26. UV/vis/NIR absorption (dashed lines) and fluorescence (solid lines) spectra of **38** in (a) $CHCl_3$ and (b) viscous solvents and **40** in (c) $CHCl_3$ and (d) viscous solvents. Reprinted with permission from ref. 56 Copyright 2018 RSC.

The presence of rotational isomers exhibiting different absorption spectra were also supported by the TDDFT calculations. As shown in Fig. 27, four model rotational isomers, which possess an s-*trans* (**38A**) and s-*cis* (**38B**) orientations of the bithienyl moiety and perpendicular orientations between the thienyl substituent and PPAB moiety (**38C** and **38D**)

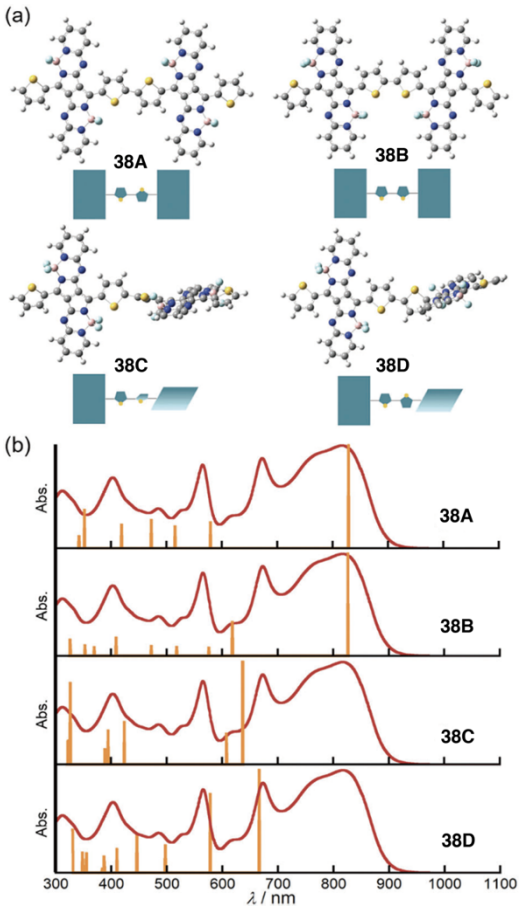

Fig. 27. (a) Optimized model structures and schematic representations. (b) Theoretical absorption of each model structure at the B3LYP/6-31G(d) level (orange bars) and the observed absorption spectra of **38** in $CHCl_3$ (red line). Redrawn with permission from ref. 56 Copyright 2018 RSC.

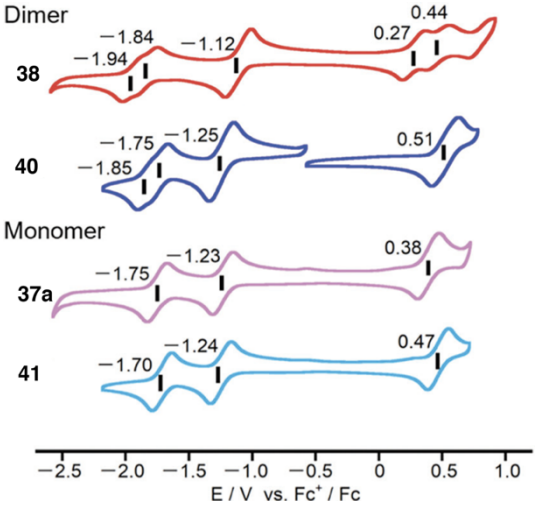

Fig. 28. Cyclic voltammograms of PPAB dimers (**38** and **40**) and monomers (**37a** and **41**) in *o*-dichlorobenzene (0.5 mM) containing 0.1 M tetra-*n*-butylammonium perchlorate as a supporting electrolyte at a scan rate of 100 mV s^{-1}. Values are half-wave potentials. Redrawn with permission from ref. 56 Copyright 2018 RSC.

reproduced the NIR absorption at 817 nm and the monomer-like absorption at 674 nm, respectively. Although various types of rotational isomers can exist in solution, the high reproducibility of these TDDFT calculations is indicative of contribution of the rotational isomerism not only around the thiophene–thiophene bond, but also around the thiophene–PPAB bond to the observed panchromatic absorption of **38**.

In response to the changes upon dimerization, the oxidation and reduction potentials of **38** shifted to the negative and positive, respectively, from those of **37a**, whereas both redox potentials were almost retained in the cases of **40** and **41** (Fig. 28).

4. Synthesis of N-confused porphyrin-aza-dipyrrin chimera and its unique tautomerism for versatile metal coordination

As a unique class of lactam structures, a porphyrin derivative can also be utilized for the Schiff base forming reaction. N-confused porphyrin (NCP)[60,61] is a kind of isomeric porphyrins[62] bearing an inverted pyrrole ring linked to the macrocycle at the α and β positions. Because of the presence of this so-called confused pyrrole ring, depending on solvent polarities NCP can take two NH tautomeric forms, namely **inner-2H-from** and **inner-3H-form** (Fig. 29),[63,64] which enable NCP to function as divalent (–2) and trivalent (–3) ligand, respectively. By merging an aza-dipyrrin-like structure with NCP, this NH tautomerism was found to be further enhanced because the *meso*-imino nitrogen atom of the aza-dipyrrin moiety can also function as a proton acceptor site. An NCP-aza-dipyrrin "*chimera*" molecule thus designed can take four tautomers (***A*–*D*-forms** in Fig. 29) with different inner and outer coordination properties.

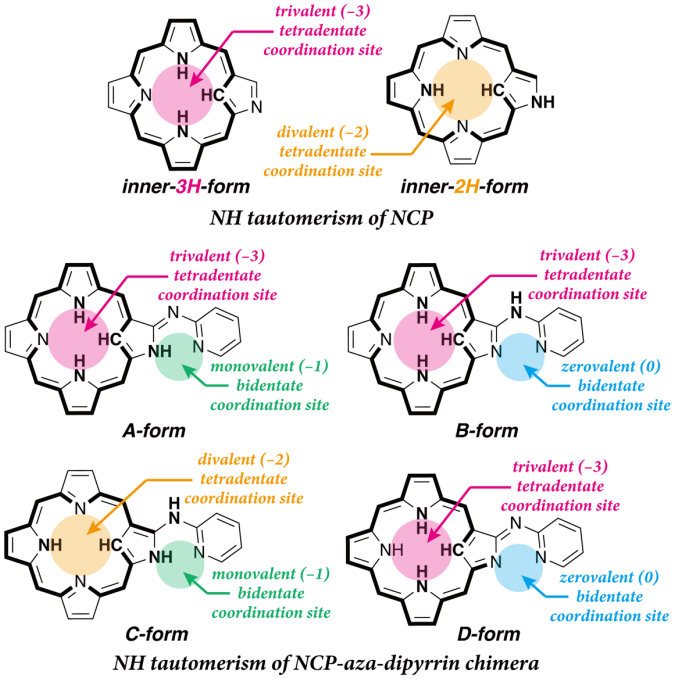

Fig. 29. Inner-2H-form and **inner-3H-form** of NCP and four possible tautomers of NCP-aza-dipyrrin chimera (***A*–*D*-forms**) and their coordination properties. Main conjugation pathways are highlighted with thick lines.

A free base form of N-confused oxoporphyrin **42**[65] was reacted with 2-aminopyridine derivatives in the presence of $TiCl_4$ and TEA to afford the NCP-aza-dipyrrin chimera **43** (Scheme 12).[26] Among four tautomers, three of them (***A*–*C*-**

forms) have been isolated as stable forms by metal coordination (**44** and **45: *A*-form**, **46: *B*-form**, and **47: *C*-form** in Scheme 13) and characterized by X-ray diffraction analysis (Fig. 30). Owing to the cross-conjugated system of ***C*-form**, which is similar to that of **inner-2H-form** of normal NCP, **47** exhibited different absorption spectral features from those of other compounds (**44**–**46**). Although ***D*-form**, which is supposed to stabilize +4 oxidation state of metal ions, has not yet been realized, NCP-aza-dipyrrin chimera can be regarded as a versatile "chameleon" ligand, which can be potentially utilized for catalytic reactions.

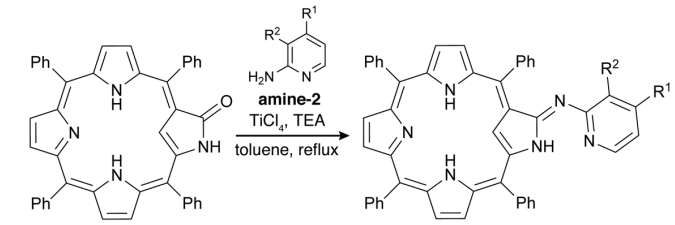

N-confused oxoporphyrin 42 **NCP-aza-dipyrrin chimera 43**

amine-2a, **43a:** $R^1 = R^2 = H$
amine-2b, **43b:** $R^1 = OMe$, $R^2 = H$
amine-2c, **43c:** $R^1 = H$, $R^2 = OCH_2CH(C_6H_{13})C_8H_{17}$

Scheme 12. Synthesis of NCP-aza-dipyrrin chimera **43**.

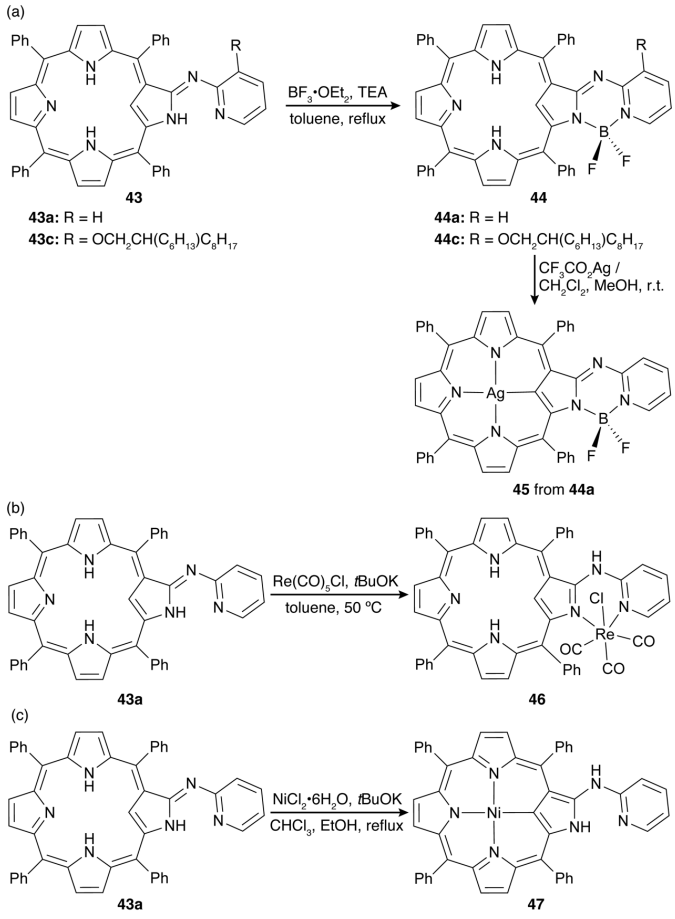

Scheme 13. Metal complexation of NCP-aza-dipyrrin chimera **43**.

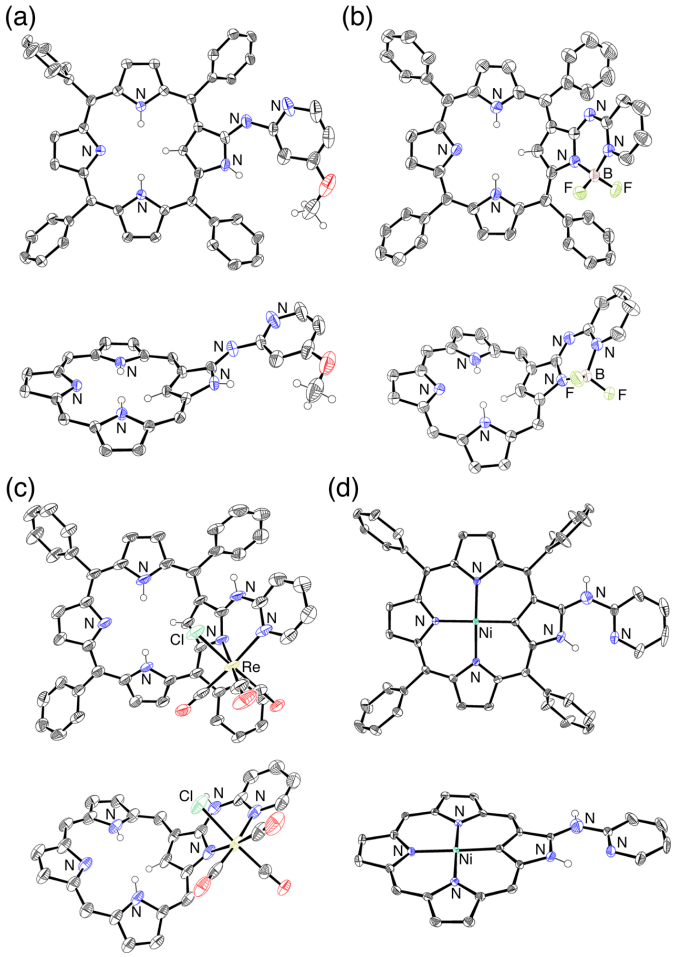

Fig. 30. X-ray single crystal structures of (a) **43b**, (b) **44c**, (c) **46** and (d) **47**, top view (top) and side view (bottom). The thermal ellipsoids are scaled to the 50% probability. Hydrogen atoms except for the NH and inner CH of pyrrole rings and the NH at the *meso*-position of the aza-dipyrrin moiety in both views, *meso*-phenyl groups in the side views and the alkoxy substituent of **44c** in both views are omitted for clarity. Reprinted with permission from ref. 26 Copyright 2019 Wiley.

5. Application studies of PPABs and its related analogues

5.1 PPABs with aggregation-induced emission enhancement properties

Despite the intense fluorescence of PPABs in solution, their fluorescence is virtually quenched in the solid state. To solve this aggregation-caused quenching (ACQ) problem, Wang et al. examined introduction of triphenylethylene as an aggregation-induced emission (AIE) generator as well as a bulky substituent to prevent compact packing and strong π-π stacking interactions.[66] Symmetric and asymmetric PPABs bearing triphenylethylene units on the benzothiazole moieties (**48** and **49**) and their reference compound (**23b**) were synthesized (Fig. 31). The synthesis of the asymmetric compound (**48**) was achieved by isolating a half-PPAB derivative and utilizing it as a starting material for the second Schiff base forming reaction.

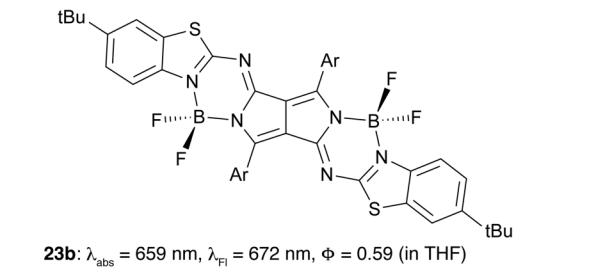

23b: λ_{abs} = 659 nm, λ_{Fl} = 672 nm, Φ = 0.59 (in THF)

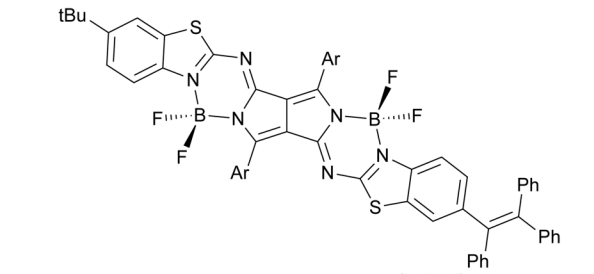

48: λ_{abs} = 668 nm, λ_{Fl} = 683 nm, Φ = 0.008 (in THF)
Φ = 0.22 (in CH_2Cl_2/hexane = 1:9)

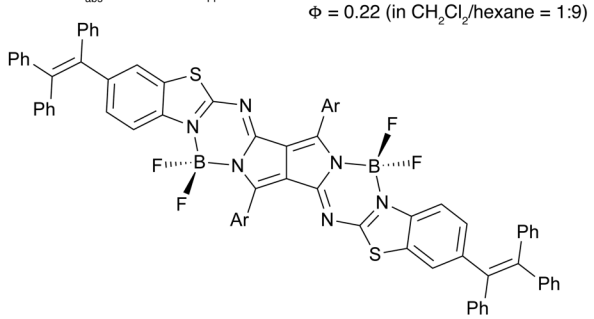

49: λ_{abs} = 677 nm, λ_{Fl} = 691 nm, Φ = 0.011 (in THF)
Φ = 0.19 (in CH_2Cl_2/hexane = 1:9)

Fig. 31. Structures of AIE-active PPABs **48** and **49** and its reference compound (**23b**). λ_{abs} and λ_{fl} are absorption and fluorescence maxima in a THF solution.

In addition to gradual red-shifts of the absorption and fluorescence, the fluorescence quantum yields in a THF solution dramatically dropped from **23b** (Φ = 0.59) to **48** (0.008) and **49** (0.011) due to enhanced non-radiative decay process by the rotation of the triphenylethylene units. In contrast, in a poor solvent system consisting of a variable ratio of dichloromethane and hexane, the emission of **48** and **49** significantly intensified up to 93-fold and 70-fold increases, respectively, at the hexane fraction of 90% compared with those in dichloromethane (Fig. 32). The fluorescence quantum yields of 0.22 for **48** and 0.19 for **49** were recorded in the aggregated state.

After confirming photostability of PPABs under continuous irradiation of 365 nm light, which caused only marginal depletion of the main absorbance by 0.14%–1.47%, which is much smaller than 21% decrease of the intensity of indocyanine green (ICG) under the same conditions, Wang et al. utilized the nanoparticles (NPs) of AIE-active PPABs for bioimaging study. The PPAB NPs, **48-NP** and **49-NP**, with average diameters of 41 nm and 22 nm, respectively, were prepared by nanoprecipitation in the presence of Pluronics F127 as a stabilizer.[67] Biocompatibility of these NPs on HeLa cell were tested using the CCK8 assay. After incubation of HeLa cell with **48-NP** for 12 h, strong fluorescence was observed in the cytoplasm using confocal fluorescence microscopy, and the intensity was further enhanced upon extension of incubation time (Fig. 33). On the other hand, only a weak fluorescence was observed in a control cell imaging experiment using nanoparticles of non AIE-active **23b**.

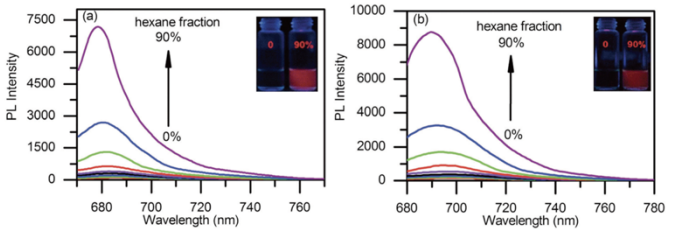

Fig. 32. Fluorescence spectra of (a) **48** and (b) **49** (10 μM) in various hexane fraction of CH_2Cl_2-hexane mixtures. Inset: Photographs of solutions in CH_2Cl_2 (left) and CH_2Cl_2/hexane = 1:9 (right) under irradiation by 365 nm light. Redrawn with permission from ref. 66 Copyright 2017 RSC.

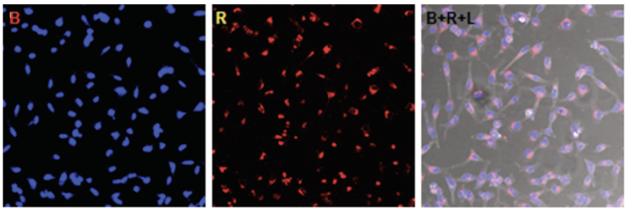

Fig. 33. Real-time fluorescence images showing **48-NP** (50 μM) stained HeLa cells at room temperature. "B" (left): cell nuclei stained by 4',6-diamidino-2-phenylindole (DAPI), "R" (middle): red fluorescence image of **48-NP** and "L": bright field, respectively. Reprint with permission from ref. 66 Copyright 2017 RSC.

5.2 Two-photon fluorescent probe

Ng et al. focused on PPABs as a potential two photon absorption (TPA)[68–70] material. Considering that donor-π-donor quadrupole structures generally exhibit high TPA cross-sections, they designed and synthesized PPABs bearing dialkylamino- and diarylamino-phenylethynyl groups (**50**, Fig. 34).[71]

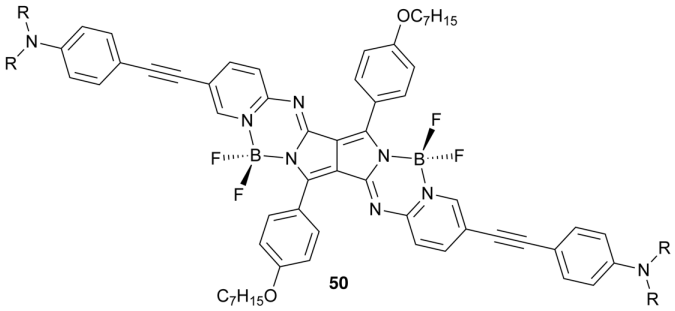

50a: R = CH_3, λ_{abs} = 696 nm, λ_{Fl} = 720 nm, Φ = 0.08, $\sigma^{(2)}$ = 800 GM ex. at 1040 nm
50b: R = Ph, λ_{abs} = 693 nm, λ_{Fl} = 715 nm, Φ = 0.14, $\sigma^{(2)}$ = 2349 GM ex. at 1040 nm

Fig. 34. Structures of TPA-active PPABs **50** and optical properties in toluene.

The lowest one-photon absorption band of **50a** and **50b** moderately shifted to the red at around 690 nm, whereas the fluorescence spectra became structureless with rather small fluorescence quantum values of 0.08 for **50a** and 0.14 for **50b** and relatively large Stokes shifts due to an intramolecular charge-transfer character. The TPA cross-sections ($\sigma^{(2)}$) were studied based on two photon excited fluorescence (TPEF) method in toluene with Rhodamine B as a standard,[72] and the $\sigma^{(2)}$ values were estimated to be 800 GM for **50a** and 2349 GM for **50b**, which are higher than that of DPP.[73,74] It was also found that at much shorter wavelength excitation (≤770 nm), which corresponds to the one-photon absorption at around 350 nm,

TPA properties became maximized. This behaviour is typical for centrosymmetric chromophores, for which selection rules for one-photon absorption and two-photon absorption become reversed.[73,74] These compounds exhibited two-photon photo luminescence (TPPL) at around 710 nm with its brightness ($\sigma^{(2)}\Phi$) of 64 GM for **50a** and 329 GM for **50b**.

Owing to the high $\sigma^{(2)}$ values and brightness, which directly relates to the two-photon fluorescence imaging efficiency, Ng et al. synthesized water-soluble PPABs (**52**–**54**) with directing triphenylphosphonium and morpholine groups to mitochondria and lysosomes, respectively, by click reactions (Scheme 14).

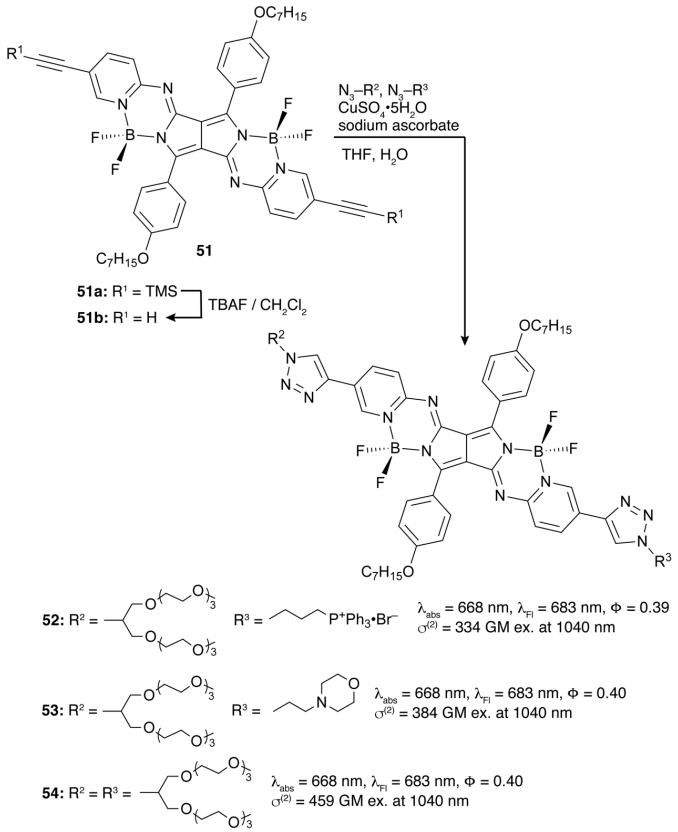

Scheme 14. Synthesis of hydrophilic PPABs **52**–**54** and optical properties in deionised water (with 0.3% v/v Tween 80 and 1% v/v DMF).

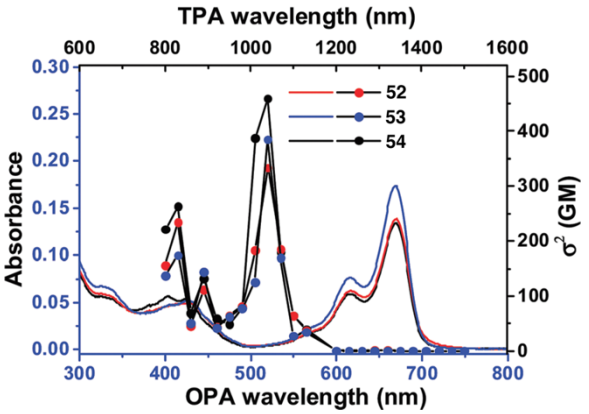

Fig. 35. Two-photon (segmented lines) and one-photon (solid lines) absorption spectra of **52**–**54** in deionised water containing 0.3% v/v Tween 80 and 1% v/v DMF. Redrawn with permission from ref. 71 Copyright 2018 RSC.

As with **50**, these compounds also showed TPA properties with maximum $\sigma^{(2)}$ of 334–459 GM (at 1040 nm) in an aqueous medium composed of deionised water with 0.3% Tween 80 and 1% DMF (Fig. 35).

Subcellular localisation studies based on the one-photon confocal imaging of HeLa cells after incubation of these TPA chromophores with MitoTracker Green or LysoTracker Green revealed that **52** with lipophilic triphenylphosphonium moiety, which was expected to target mitochondria, localised in lysosomes, whereas the morpholine-containing **53** did not show any localization in lysosomes (Fig. 36). Ng. et al. ascribed these unexpected results to the large hydrophobic PPAB core compared to the targeting groups. Finally, they examined the two-photon fluorescent probe property of PPABs. As HeLa cells stained with **54** were observed by both one-photon and two-photon imaging (Fig. 37), they have concluded that PPAB can potentially be applied as two-photon fluorescent probe, which enables long-term imaging of cellular processes and deep tissue imaging.

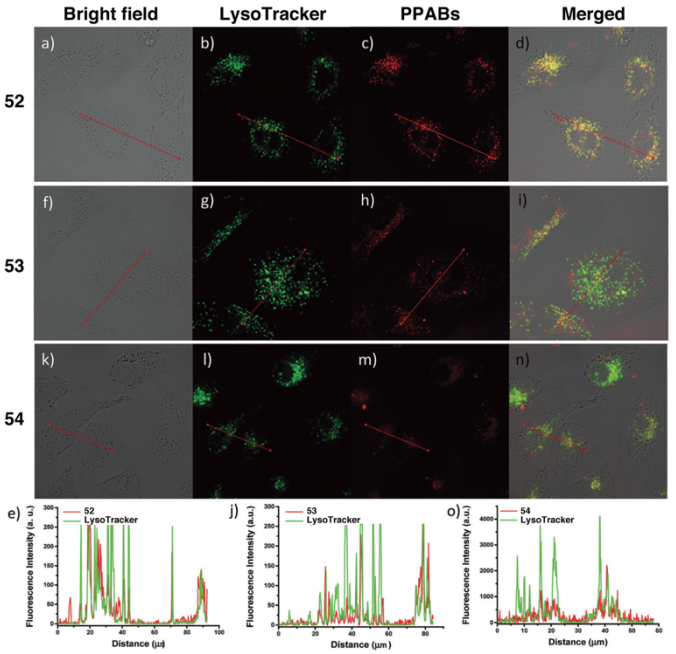

Fig. 36. Visualisation of the intracellular fluorescence of **52**–**54** (2 μM) after 4 h incubation and LysoTracker Green (1.5 μM) after 20 min incubation in HeLa cells: panels (a), (f) and (k): bright field images, panels (b), (g) and (l): fluorescence of LysoTracker Green, panels (c), (h) and (m) fluorescence of **52**–**54** and panels (d), (i) and (n) super imposed images. Panels (e), (j) and (o): fluorescence intensity profiles of PPABs (red line) and LysoTracker Green (green line) traced along the red lines in the corresponding images above. Redrawn with permission from ref. 71 Copyright 2018 RSC.

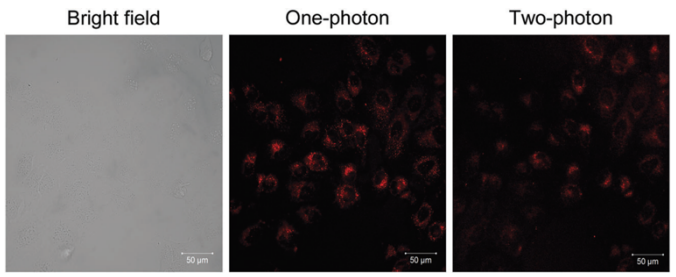

Fig. 37. One-photon (λ_{ex} = 633 nm, λ_{em} = 650–735 nm) and two-photon (λ_{ex} = 633 nm, λ_{em} = 650–735 nm) images of HeLa cells stained by **54**. Reprinted with permission from ref. 71 Copyright 2018 RSC.

5.3 Photoacoustic imaging and photothermal cancer therapy

Photoacoustic imaging (PAI) has been gathering attention as one of the most powerful imaging technics.[75,76] The following properties are reported to be required for PA contrasting agents for *in vivo* use; (i) high molar extinction coefficient in the NIR region from 700 to 900 nm referred to as optical window and (ii) efficient conversion of excited photoenergies to thermoelastic expansion. From these viewpoints, Miki and we expected that PPABs can be a potential candidate as a PA imaging agent because of their intense absorption in the NIR region and non-fluorescent nature in aggregated states.

To endow biocompatibility and achieve self-assembled structures, PEGylated PPAB **55** was synthesized (Fig. 38).[77] In water, **55** formed two kinds of spherical self-assemblies with diameters of ~20 nm and 70–100 nm, respectively. Since no layered structure was observed by TEM, micelles and multimicellar aggregates were inferred. In contrast to the intense absorption and fluorescence in DMF, the absorption spectrum became broad and the fluorescence was virtually quenched in water (Fig. 39). A PA tumour-imaging of **55** was not carried out in this study, because of its rather higher critical aggregation concentration value than other BODIPY analogues tested in this study,[78] which becomes a drawback for efficient accumulation in tumour tissues by the EPR effect. However, **55** exhibited better PA signals (47 V/J•abs at 720 nm and 49 V/J•abs at 790 nm) compared to the conventional ICG dye (PA/PA_{ICG} at 720 nm of 1.23 and at 790 nm of 1.08).[79]

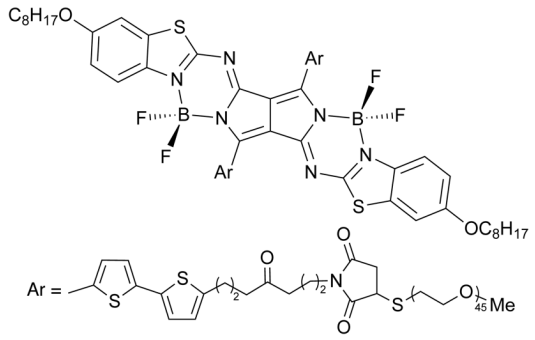

Fig. 38. A structure of PEGylated PPAB **55**.

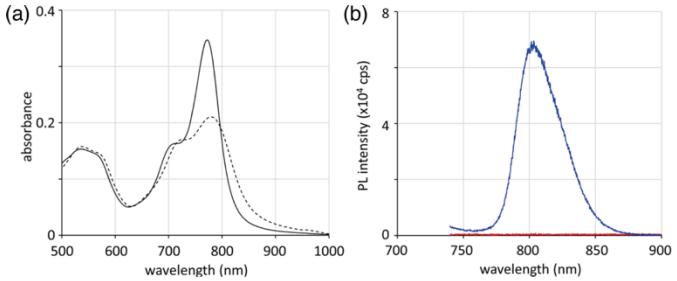

Fig. 39. (a) vis/NIR absorption spectra (0.1 mg/mL) of **55** in DMF (solid line) and water (dashed line). (b) Photoluminescence spectra (λ_{ex} = 720 nm) of **55** in DMF (blue line) and water (red line). Redrawn with permission from ref. 77 Copyright 2017 ACS.

Very recently, Sun, Shao and Dong et al. reported that NPs of normal PPAB exhibited not only PA response, but also photothermal therapy (PTT) activity.[80] PPAB **28a**, which was synthesized in our study as a second-generation PPAB, was converted into NPs (**28a-NPs**) with an average particle size of 90 ± 7 nm by reprecipitation method (Fig. 40a). **28a-NPs** in aqueous solution exhibited red-shifted absorption from **28a** in dichloromethane, which covered broad ranges between 500 and 800 nm (Fig. 40b). Owing to the high photothermal

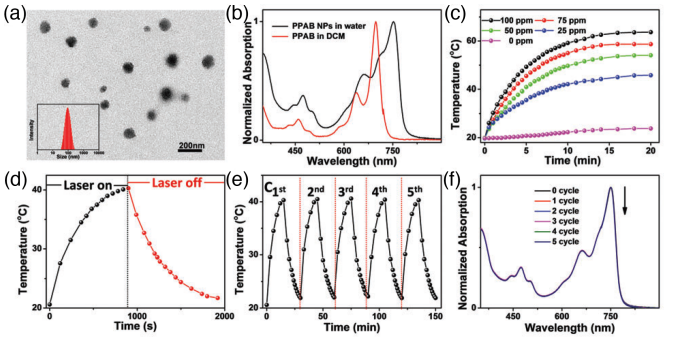

Fig. 40. (a) TEM image of **28a-NPs**. Inset: diameter distribution. (b) UV/vis/NIR absorption spectra of **28a** in CH_2Cl_2 and **28a-NPs** in water. (c) Temperature elevation curves of **28a-NPs** at different concentrations under irradiation of 730 nm laser (0.75 W cm^{-2}). (d) Photothermal response of **28a-NPs** in an aqueous solution (25 ppm) under irradiation of 730 nm laser (0.75 W cm^{-2}) for 15 min and after the laser was turned off. (e) Temperature profiles of **28a-NPs** in an aqueous solution for five alternative ON/OFF cycles. (f) UV/vis/NIR absorption spectra of **28a-NPs** after each ON/OFF cycle. Reprinted with permission from ref. 80 Copyright 2017 RSC.

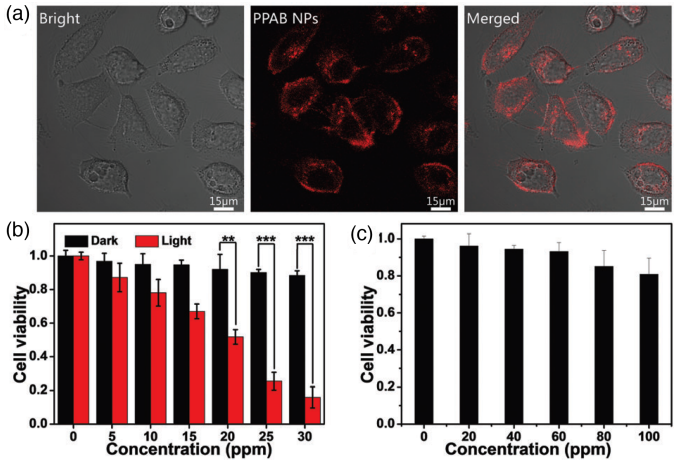

Fig. 41. (a) Confocal microscopy images of HeLa cells incubated with **28a-NPs** (60 ppm) for 12 h. (b) Relative viabilities of HeLa cells after incubation with various concentration of **28a-NPs** (730 nm laser, 0.75 W cm^{-2}, 5 min, mean ± SD, n = 5, $^{**}P < 0.01$, $^{***}P < 0.001$). (c) Relative viabilities of HeLa cells after incubation with various concentrations of **28a-NPs** for 24 h. Reprinted with permission from ref. 80 Copyright 2017 RSC.

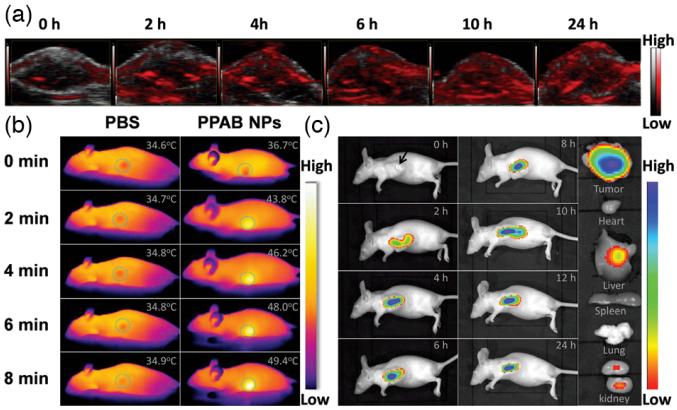

Fig. 42. (a) *In vivo* PA images in tumour sites after intravenous injection of **28a-NPs** (50 ppm, 100 μL). (b) Photothermal images of tumour-bearing mice exposed to laser irradiation for 8 min after the injection of PBS or **28a-NPs**. (c) Fluorescence images of living mice bearing xenograft HeLa tumours at 0, 2, 4, 6, 8, 10, 12 and 24 h post-injection of **28a-NPs**. Reprinted with permission from ref. 80 Copyright 2017 RSC.

conversion (PTC) efficiency, which was estimated to be 47%[81] (Fig. 40c and d) and good photostability (Fig. 40e and f), clinical PTT application of **28a-NPs** was demonstrated.

Using HeLa cells as tumour cell model, bio-imaging property and PTT performance of **28a-NPs** *in vitro* were examined. As shown in Fig. 41a, **28a-NPs** were dispersed in the cell cytoplasm and effectively up-taken in the HeLa cells. The MTT assay revealed low-toxicity of **28a-NPs** in the dark and obvious cytotoxity under exposure of 730 nm laser illumination (Fig. 41b and c). With these results in hand, *in vivo* imaging and PTT ability of **28a-NPs** were exmamined using the HeLa tumour-xenograft model. **28a-NPs** successfully accumulated in the tumour tissue, which enabled both PAI (Fig. 42a) and NIR fluorescence imaging (NIR-FI) (Fig. 42c). The photothermal image revealed that the temperature of the tumour sites reached to 49.4 ˚C, which is high enough to kill tumour cells (Fig. 42b). After 8 treatment cycles consisting of injection of **28a-NPs** every other day and laser irradiation (730 nm, 0.75 W cm^{-2}, 5 min) for 6 hours after NPs administration, tumours of mice in the treatment group were effectively ablated without any skin damage (Fig. 43a–c). On the other hand, rapid growth of the tumour size was observed for mice in the control group with administration of PBS only and in the comparison groups with laser irradiation only or administration of NPs only. The steady increase of body weight further demonstrated no evident toxicity and excellent biocompatibility of **28a-NPs** (Fig. 43d). These results obviously indicated that NPs of PPABs can serve as an efficient dual-mode (PAI and NIR-FI) imaging-guided PTT agents.

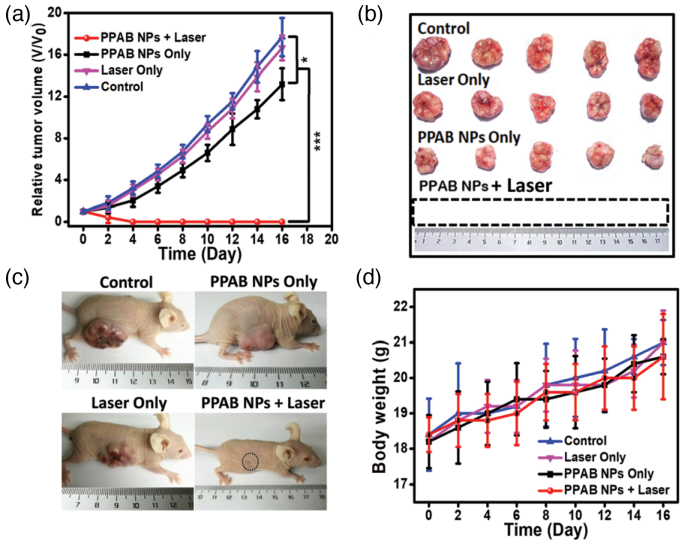

Fig. 43. (a) Tumour growth of various groups. Tumour volumes have been normalized to the initial sizes (mean ± SD, n = 5, *P < 0.05, ***P < 0.001). (b) Photographs of excised tumours after various treatments. (c) Photographs of mice after 16 days treatment. (d) Body weight of various treatment groups. Reprinted with permission from ref. 80 Copyright 2017 RSC.

5.4 Organic photovoltaics

In addition to the above-mentioned application of PPABs in the fields of bioimaging and therapeutics, PPABs and aza-BODIPY analogues can be regarded as potential candidates for organic photovoltaics considering their highly conjugated structures with reversible redox properties and prominent absorption in the vis/NIR regions.[82] To assess performance as an OPV material, time-resolved microwave conductivity (TRMC)[83] measurements on a series of PPABs,[47] PPAB dimers,[56] BDAB and IDAB[25] were performed using monochromatic light pulse from a nano-second laser (laser-flash)[84] or white-light pulse from a Xe flash-lamp (Xe-flash)[85] as photoexcitation sources. Among PPABs, **22a**

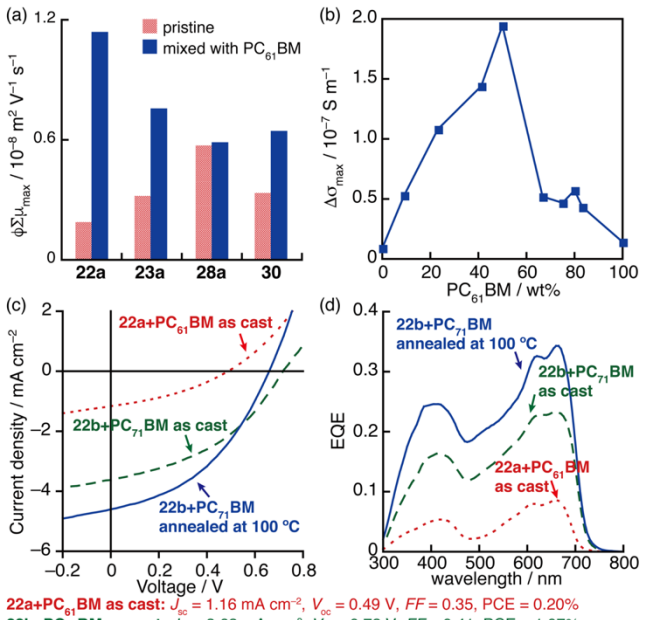

Fig. 44. (a) Maximum TRMC signals ($\phi\Sigma\mu_{max}$) of pristine PPAB molecules and PPAB/$PC_{61}BM$ (1:1 (w/w)) drop-cast films from chloroform solutions measured by laser-flash TRMC (ex. 355 nm); (b) $\Delta\sigma_{max}$ of Xe-flash TRMC of drop-cast films of **22a**:$PC_{61}BM$ plotted as a function of $PC_{61}BM$ content. 100wt% $PC_{61}BM$ represents pure $PC_{61}BM$; (c) J/V curves of the PPAB/$PC_{61(71)}BM$ (1:1 (w/w)) (dotted line: **22a**/$PC_{61}BM$, spin-coated from a $CHCl_3$ solution containing 0.7 v/v% DIO without thermal annealing; dashed line: **22b**/$PC_{71}BM$, spin-coated from a $CHCl_3$ solution containing 0.5 v/v% DIO without thermal annealing; solid line: **22b**:$PC_{71}BM$, spin-coated from a $CHCl_3$ solution containing 0.5 v/v % DIO with 100 ˚C annealing) ; (d) EQE spectra of the devices of (c). Redrawn with permission from ref. 47 Copyright 2015 Wiley.

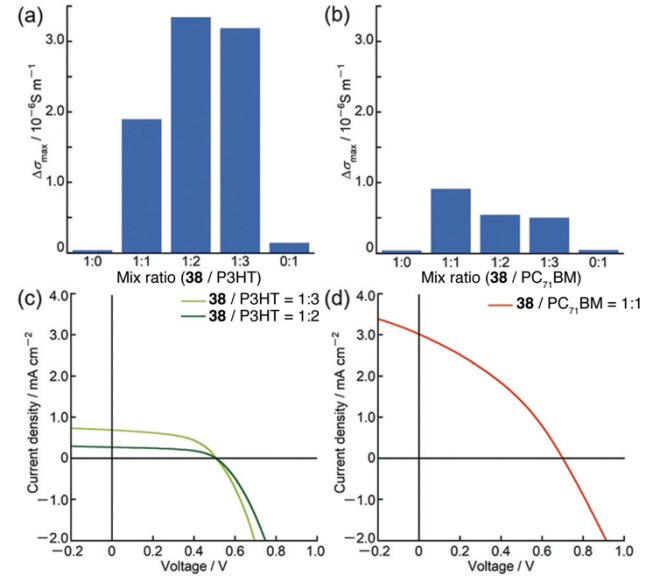

Fig. 45. Maximum Xe-flash TRMC signals ($\Delta\sigma_{max}$) of (a) **38**/P3HT and (b) **38**/$PC_{71}BM$ drop-cast films with various mixing ratios, and J/V curves of (c) **38**/P3HT cells (1:3 (w/w), pale green line and 1:2 (w/w), green line, spin-coated from *o*-dichlorobenzene solution) and (d) **38**/$PC_{71}BM$ cells (1:1 (w/w), red line, spin-

coated from chloroform solution containing 0.5 v/v% DIO). Redrawn with permission from ref. 56 Copyright 201087 RSC.

bearing pyridine moieties and phenyl groups as heteroaromatic rings and aryl-substituents of the DPP moiety, respectively, exhibited potential p-type response with significant enhancement of the maximum transient conductivity, $\phi\Sigma\mu_{max}$, in which ϕ and $\Sigma\mu$ represent charge carrier generation efficiency and the sum of the hole and electron mobilities, respectively, upon blending with $PC_{61}BM$ as an n-type material (Fig. 44a). After optimization of the substituents of PPAB and device fabrication methods (Fig. 44b), the best OPV performance with a power conversion efficiency (PCE) of 1.27%, open-circuit voltage (V_{oc}) of 0.66 V, short-circuit current density (J_{sc}) of 4.60 mA cm^{-2} and fill factor (*FF*) of 0.42 was achieved by an inverted cell structure (Glass/ITO/ZnO/BHJ/MoO_3/Ag) consisting of a blended film of a 1:1 (w/w) mixture of **22b** and $PC_{71}BM$ as an active bulk-heterojunction (BHJ) layer (Fig. 44c and d). In the cases of BDAB and IDAB, n-type properties were expected based on the TRMC measurements, but device fabrication has not been attempted because $\phi\Sigma\mu_{max}$ of blended films of BDAB and IDAB with P3HT were less than a half of that of pristine P3HT.

In addition to the p-type properties, the PPAB dimer (**38**) exhibited n-type property based on the TRMC analysis and electrochemical measurements. Upon excitation using Xe-flash, significant enhancement of the maximum transience conductivity, $\Delta\sigma_{max}$, which correlates with the charge separation efficiency and the sum of hole and electron mobilities, was observed for both blended films of **38** and P3HT and $PC_{71}BM$ (Fig. 45a and b). Despite the low PCEs and small J_{sc} of the BHJ-OPV device with an inverted cell structure (glass/ITO/ZnO/ BHJ/MoO_3/Ag) due to the low solubility of **38** (Fig. 45c and d), it is of interest that the panchromatic PPAB dimer can show photovoltaic performance as both p- and n-type materials.

Conclusions

In this feature article, aza-BODIPY analogues synthesized by the Schiff base forming reaction of lactams and heteroaromatic amines and their related analogues are surveyed. In addition to benzo[*c*,*d*]indole and 3-iminoisoindolin-1-one as simple mono-lactam structures, bis-lactam compounds, such as DPP, benzodipyrrolidone and isoindigo, were successfully converted to the corresponding aza-BODIPY structures. Furthermore, a lactam moiety embedded in a large macrocycle like N-confused porphyrin can also be activated under the Schiff base forming reaction conditions to afford NCP-aza-dipyrrin chimera with unique NH tautomerism for versatile metal coordination. As a new functional chromophore, various application studies of PPABs have been intensively carried out not only in the fields of imaging and therapy, but also in the fields of organic electronics. Thanks to the NIR absorption and fluorescence, and photothermal conversion, a variety of imaging techniques including AIE imaging, NIR-FI and PAI, become available using PPAB chromophores. In combination with NIR-FI and PAI, the initial trial of PPABs as dual-mode imaging-guided PTT agents was achieved. Further optimization of peripheral substituents and PPAB structures towards selective targeting of cancer cells in deeper tissues will be the next research topics. As for the organic electronics, due to several reasons, the PCE is not so high as expected. In addition to detailed optimization of the chromophore structures for BHJ-OPV devices, it will also be an important research direction to apply aza-BODIPY chromophores for other photovoltaics, such as dye-sensitized solar cells (DSSC) and perovskite solar cells. Last but not least, organic light emitting diode (OLED) application will be of future interest.

Since our first report on the synthesis of PPABs in 2013, both synthetic chemistry and application studies of their aza-BODIPY family have been rapidly developed owing to the facile synthesis, ready availability of lactam and heteroaromatic amine precursors and fine-tuning of optical and electrochemical properties. Taking these advantages, aza-BODIPY synthesis based on the Schiff base forming reaction protocol will be utilized in a greater variety of research fields. As an investigator of this field, I will contribute to its further growth and enjoy prosperous future of this chemistry.

Conflicts of interest

There are no conflicts to declare.

Acknowledgements

This work was supported by Grants-in-Aid for Scientific Research (B) (JSPS KAKENHI Grant no. JP19H02703), Grant-in-Aid for Challenging Exploratory Research (JSPS KAKENHI Grant no. JP18K19081) and Scientific Research on Innovative Areas, "π-System Figuration: Control of Electron and Structural Dynamism for Innovative Functions (no. 2601)" (JSPS KAKENHI Grant no. JP15H01001 and JP17H05160) and "New Polymeric Materials Based on Element-Blocks (no. 2401)" (JSPS KAKENHI Grant no. 25102503 and JP15H00756).

Author Profile: *Soji Shimizu was born in Kyoto, Japan, in 1979. He graduated from Kyoto University in 2002 and obtained his PhD there under the supervision of Professor Atsuhiro Osuka in 2007 for his research on the syntheses and properties of expanded porphyrins. During his PhD studies, he made a short stay in the group of Professor Jonathan L. Sessler, the University of Texas at Austin in 2005. He was appointed as an assistant professor in 2006 and a lecturer in 2010 at Department of Chemistry, Graduate School of Science, Tohoku University and started his academic career in the group of Professor Nagao Kobayashi in the field of phthalocyanine chemistry. He was then promoted to an associate professor at Department of Chemistry and Biochemistry, Graduate School of Engineering, Kyushu University in 2014. His research interests cover the synthesis of conjugated molecules with novel structures and their optical and electrochemical properties.*

Notes and references

1 (a) A. Loudet and K. Burgess, in *Handbook of Porphyrin Science*, eds. K. M. Kadish, K. M. Smith and R. Guilard, World Scientific Publishing, Singapore, 2010, pp. 1-164; (b) A. Loudet and K. Burgess, *Chem. Rev.*, 2007, **107**, 4891.

2 G. Ulrich, R. Ziessel and A. Harriman, *Angew. Chem. Int. Ed.*, 2008, **47**, 1184.

3 (a) T. E. Wood and A. Thompson, *Chem. Rev.*, 2007, **107**, 1831; (b) T. E. Wood, M. I. Uddin and A. Thompson, in *Handbook of Porphyrin Science*, eds. K. M. Kadish, K. M. Smith and R. Guilard, World Scientific Publishing, Singapore, 2010, pp. 235-292.

4 R. P. Haughland, *Handbook of Fluorescent Probes and Research Products*, Molecular Probes, Inc., Eugene, OR, 2002.

5 Y. Ni and J. Wu, *Org. Biomol. Chem.*, 2014, **12**, 3774.

6 Y. Urano, D. Asanuma, Y. Hama, Y. Koyama, T. Barrett, M. Kamiya, T. Nagano, T. Watanabe, A. Hasegawa, P. L. Choyke and H. Kobayashi, *Nat. Med.*, 2009, **15**, 104.

7 (a) A. C. Benniston and G. Copley, *Phys. Chem. Chem. Phys.*, 2009, **11**, 4124; (b) N. Boens, V. Leen and W. Dehaen, *Chem. Soc. Rev.*, 2012, **41**, 1130; (c) S. T. Manjare, J. Kim, Y. Lee, and D. G. Churchill, *Org. Lett.,* 2014, **16**, 520.

8 (a) A. Costela, I. García-Moreno, C. Gomez, R. Sastre, F. Amat-Guerri, M. Liras, F. López Arbeloa, J. Bañuelos Prieto and I. López Arbeloa, *J. Phys. Chem. A*, 2002, **106**, 7736; (b) D. Zhang, V. Martin, I. Garcia-Moreno, A. Costela, M. E. Perez-Ojeda and Y. Xiao, *Phys. Chem. Chem. Phys.*, 2011, **13**, 13026.

9 A. Kamkaew, S. H. Lim, H. B. Lee, L. V. Kiew, L. Y. Chung and K. Burgess, *Chem. Soc. Rev.*, 2013, **42**, 77.

10 (a) L. Bonardi, H. Kanaan, F. Camerel, P. Jolinat, P. Retailleau and R. Ziessel, *Adv. Funct. Mater.*, 2008, **18**, 401; (b) A. Bessette and G. S. Hanan, *Chem. Soc. Rev.,* 2014, **43**, 3342.

11 H. Klfout, A. Stewart, M. Elkhalifa and H. He, *ACS Appl. Mater. Interfaces*, 2017, **9**, 39873.

12 D. Holten, D. F. Bocian and J. S. Lindsey, *Acc. Chem. Res.*, 2001, **35**, 57.

13 (a) H. Lu, J. Mack, Y. Yang and Z. Shen, *Chem. Soc. Rev.*, 2014, **43**, 4778; (b) X.-D. Jiang, S. Li, J. Guan, T. Fang, X. Liu and L.-J. Xiao, *Curr. Org. Chem.,* 2016, **20**, 1736.

14 (a) M. A. T. Rogers, *J. Chem. Soc.*, 1943, 590; (b) W. H. Davies and M. A. T. Rogers, *J. Chem. Soc.*, 1944, 126.

15 J. Killoran, L. Allen, J. F. Gallagher, W. M. Gallagher and D. F. O'Shea, *Chem. Commun.*, 2002, **24**, 1862.

16 (a) D. Wu, S. Cheung, M. Devocelle, L.-J. Zhang, Z.-L. Chen and D. F. O'Shea, *Chem. Commun.*, 2015, **51**, 16667; (b) A. Palma, L. A. Alvarez, D. Scholz, D. O. Frimannsson, M. Grossi, S. J. Quinn and D. F. O'Shea, *J. Am. Chem. Soc.*, 2011, **133**, 19618; (c) A. Palma, M. Tasior, D. O. Frimannsson, T. T. Vu, R. Méallet-Renault and D. F. O'Shea, *Org. Lett.*, 2009, **11**, 3638; (d) A. Loudet, R. Bandichhor, K. Burgess, A. Palma, S. O. McDonnell, M. J. Hall and D. F. O'Shea, *Org. Lett.*, 2008, **10**, 4771.

17 (a) A. Gorman, J. Killoran, C. O'Shea, T. Kenna, W. M. Gallagher and D. F. O'Shea, *J. Am. Chem. Soc.*, 2004, **126**, 10619; (b) M. Grossi, A. Palma, S. O. McDonnell, M. J. Hall, D. K. Rai, J. Muldoon and D. F. O'Shea, *J. Org. Chem.*, 2012, **77**, 9304.

18 (a) W. Zhao and E. M. Carreira, *Angew. Chem. Int. Ed. Engl.*, 2005, **44**, 1677; (b) W. Zhao and E. M. Carreira, *Chem. –Eur. J.*, 2006, **12**, 7254.

19 V. F. Donyagina, S. Shimizu, N. Kobayashi and E. A. Lukyanets, *Tetrahedron Lett.*, 2008, **49**, 6152.

20 H. Lu, S. Shimizu, J. Mack, Z. Shen and N. Kobayashi, *Chem. –Asian. J.*, 2011, **6**, 1026.

21 A. Díaz-Moscoso, E. Emond, D. L. Hughes, G. J. Tizzard, S. J. Coles and A. N. Cammidge, *J. Org. Chem.*, 2014, 8932.

22 S. R. Oakley, G. Nawn, K. M. Waldie, T. D. MacInnis, B. O. Patrick and R. G. Hicks, *Chem. Commun.*, 2010, **46**, 6753.

23 S. Shimizu, A. Murayama, T. Haruyama, T. Iino, S. Mori, H. Furuta and N. Kobayashi, *Chem. –Eur. J.*, 2015, **21**, 12996.

24 S. Shimizu, T. Iino, Y. Araki and N. Kobayashi, *Chem. Commun.*, 2013, **49**, 1621.

25 M. Tamada, T. Iino, Y. Wang, M. Ide, A. Saeki, H. Furuta, N. Kobayashi and S. Shimizu, *Tetrahedron Lett.*, 2017, **58**, 3151.

26 M. Fukuda, S. Mori, H. Furuta and S. Shimizu, *Chem. –Asian. J.*, 2019,**14**, 1697.

27 N. P. Vasilenko and F. A. Mikhailenko, *Ukr. Khim. Zh. (Ukr. Ed.)*, 1986, **52**, 308.

28 C. Cheng, N. Gao, C. Yu, Z. Wang, J. Wang, E. Hao, Y. Wei, X. Mu, Y. Tian, C. Ran and L. Jiao, *Org. Lett.*, 2014, **17**, 278.

29 N. P. Vasilenko, F. A. Mikhailenko and J. I. Rozhinsky, *Dyes Pigments*, 1981, **2**, 231.

30 (a) Y. N. Hong, J. W. Y. Lam and B. Z. Tang, *Chem. Commun.*, 2009, 4332; (b) Y. Hong, J. W. Y. Lam and B. Z. Tang, *Chem. Soc. Rev.*, 2011, **40**, 5361.

31 (a) C.-H. Zhao, A. Wakamiya, Y. Inukai and S. Yamaguchi, *J. Am. Chem. Soc.*, 2006, **128**, 15934; (b) A. Wakamiya, K. Mori and S. Yamaguchi, *Angew. Chem. Int. Ed.*, 2007, **46**, 4273.

32 U. Rösch, S. Yao, R. Wortmann and F. Würthner, *Angew. Chem. Int. Ed.*, 2006, **45**, 7026.

33 H. Liu, H. Lu, J. Xu, Z. Liu, Z. Li, J. Mack and Z. Shen, *Chem. Commun.*, 2014, **50**, 1074.

34 H. Liu, H. Lu, Z. Zhou, S. Shimizu, Z. Li, N. Kobayashi and Z. Shen, *Chem. Commun.*, 2015, **51**, 1713.

35 M. Irimia-Vladu, E. D. Glowacki, P. A. Troshin, G. Schwabegger, L. Leonat, D. K. Susarova, O. Krystal, M. Ullah, Y. Kanbur, M. A. Bodea, V. F. Razumov, H. Sitter, S. Bauer and N. S. Sariciftci, *Adv. Mater.*, 2012, **24**, 375.

36 S. Y. Qu and H. Tian, *Chem. Commun.*, 2012, **48**, 3039.

37 C. B. Nielsen, M. Turbiez and I. McCulloch, *Adv. Mater.*, 2013, **25**, 1859.

38 J. S. Zambounis, Z. Hao and A. Iqbal, *Nature*, 1997, **388**, 131.

39 M. Grzybowski and D. T. Gryko, *Adv. Optical Mater.*, 2015, **3**, 280.

40 (a) W. Li, K. H. Hendriks, A. Furlan, W. S. Roelofs, S. C. Meskers, M. M. Wienk and R. A. Janssen, *Adv. Mater.*, 2014, **26**, 1565; (b) W. Li, A. Furlan, W. S. Roelofs, K. H. Hendriks, G. W. van Pruissen, M. M. Wienk and R. A. Janssen, *Chem. Commun.*, 2014, **50**, 679; (c) W. Li, K. H. Hendriks, A. Furlan, W. S. Roelofs, M. M. Wienk and R. A. Janssen, *J. Am. Chem. Soc.*, 2013, **135**, 18942; (d) W. Li, A. Furlan, K. H. Hendriks, M. M. Wienk and R. A. Janssen, *J. Am. Chem. Soc.*, 2013, **135**, 5529; (e) K. H. Hendriks, G. H. Heintges, V. S. Gevaerts, M. M. Wienk and R. A. Janssen, *Angew. Chem. Int. Ed. Engl.*, 2013, **52**, 8341; (f) M. Kirkus, L. Wang, S. Mothy, D. Beljonne, J. Cornil, R. A. Janssen and S. C. Meskers, *J. Phys. Chem. A*, 2012, **116**, 7927; (g) J. C. Bijleveld, V. S. Gevaerts, D. Di Nuzzo, M. Turbiez, S. G. Mathijssen, D. M. de Leeuw, M. M. Wienk and R. A. Janssen, *Adv. Mater.*, 2010, **22**, E242; (h) M. M. Wienk, M. Turbiez, J. Gilot and R. A. J. Janssen, *Adv. Mater.*, 2008, **20**, 2556.

41 (a) M. Grzybowski, E. Glodkowska-Mrowka, T. Stoklosa and D. T. Gryko, *Org. Lett.*, 2012, **14**, 2670; (b) M. Grzybowski, V. Hugues, M. Blanchard-Desce and D. T. Gryko, *Chem. –Eur. J.*, 2014, **20**, 12493; (c) S. Richert, S. Mosquera Vazquez, M. Grzybowski, D. T. Gryko, A. Kyrychenko and E. Vauthey, *J. Phys. Chem. B*, 2014, **118**, 9952; (d) A. Nowak-Król, M. Grzybowski, J. Romiszewski, M. Drobizhev, G. Wicks, M. Chotkowski, A. Rebane, E. Górecka and D. T. Gryko, *Chem. Commun.*, 2013, **49**, 8368.

42 (a) A. Iqbal, M. Jost, R. Kirchmayr, J. Pfenninger, A. Rochat and O. Wallquist, *Bull. Soc. Chim. Belg.*, 1988, **97**, 615; (b) Z. M. Hao and A. Iqbal, *Chem. Soc. Rev.*, 1997, **26**, 203.

43 (a) G. M. Fischer, A. P. Ehlers, A. Zumbusch and E. Daltrozzo, *Angew. Chem. Int. Ed.*, 2007, **46**, 3750; (b) G. M. Fischer, M. Isomäki-Krondahl, I. Göttker-Schnetmann, E. Daltrozzo and A. Zumbusch, *Chem. –Eur. J.*, 2009, **15**, 4857.

44 (a) G. M. Fischer, C. Jüngst, M. Isomäki-Krondahl, D. Gauss, H. M. Möller, E. Daltrozzo and A. Zumbusch, *Chem. Commun.*, 2010, **46**, 5289; (b) G. M. Fischer, M. K. Klein, E. Daltrozzo and A. Zumbusch, *Eur. J. Org. Chem.*, 2011, **2011**, 3421; (c) S. Wiktorowski, G. M. Fischer, M. J. Winterhalder, E. Daltrozzo and A. Zumbusch, *Phys. Chem. Chem. Phys.*, 2012, **14**, 2921.

45 M. Y. Berezin, W. J. Akers, K. Guo, G. M. Fischer, E. Daltrozzo, A. Zumbusch and S. Achilefu, *Biophys. J.*, 2009, **97**, L22.

46 W. J. Akers, C. Kim, M. Berezin, K. Guo, R. Fuhrhop, G. M. Lanza, G. M. Fischer, E. Daltrozzo, A. Zumbusch, X. Cai, L. V. Wang and S. Achilefu, *ACS nano*, 2011, **5**, 173.

47 S. Shimizu, T. Iino, A. Saeki, S. Seki and N. Kobayashi, *Chem. –Eur. J.*, 2015, **21**, 2893.

48 (a) K. Kim, C. Jo, S. Easwaramoorthi, J. Sung, D. H. Kim, and D. G. Churchill, *Inorg. Chem.,* 2010, **49**, 4881; (b) N. Maiti, J. Lee, S. J. Kwon, J. Kwak, Y. Do, D. G. Churchill, *Polyhedron,* 2006, **25**, 1519.

49 W. B. Cui, J. Yuen and F. Wudl, *Macromolecules*, 2011, **44**, 7869.

50 Y. Wang, L. Chen, R. El-Shishtawy, S. Aziz and K. Müellen, *Chem. Commun.*, 2014, **50**, 11540.

51 E. Wang, W. Mammo and M. R. Andersson, *Adv. Mater.*, 2014, **26**, 1801.

52 M. Nakamura, H. Tahara, K. Takahashi, T. Nagata, H. Uoyama, D. Kuzuhara, S. Mori, T. Okujima, H. Yamada and H. Uno, *Org. Biomol. Chem.*, 2012, **10**, 6840.

53 W. Yue, T. He, M. Stolte, M. Gsanger and F. Würthner, *Chem. Commun.*, 2014, **50**, 545.

54 G. M. Fischer, E. Daltrozzo and A. Zumbusch, *Angew. Chem. Int. Ed.*, 2011, **50**, 1406.

55 A. Wakamiya, T. Murakami and S. Yamaguchi, *Chem. Sci.*, 2013, **4**, 1002.

56 Y. Kage, S. Mori, M. Ide, A. Saeki, H. Furuta and S. Shimizu, *Mater. Chem. Front.*, 2018, **2**, 112.

57 M. U. Winters, J. Kärnbratt, M. Eng, C. J. Wilson, H. L. Anderson and B. Albinsson, *J. Phys. Chem. C*, 2007, **111**, 7192.

58 H. Doan, S. L. Raut, D. Yale, M. Balax, S. V. Dzyuba and Z. Gryczynski, *Chem. Commun.*, 2016, **52**, 9510.

59 K. H. Park, S. Ooi, T. Kim, T. Tanaka, A. Osuka and D. Kim, *Phys. Chem. Chem. Phys.*, 2016, **18**, 23374.

60 H. Furuta, T. Asano and T. Ogawa, *J. Am. Chem. Soc.*, 1994, **116**, 767.

61 P. J. Chmielewski, L. Latos-Grażyński, K. Rachlewicz and T. Głowiak, *Angew. Chem. Int. Ed. Engl.*, 1994, **33**, 779.

62 (a) J. L. Sessler, Z. Gross and H. Furuta, *Chem. Rev.*, 2017, **117**, 2201; (b) J. L. Sessler and S. J. Weghorn, *Expanded, Contracted, and Isomeric Porphyrins*, Pergamon Press, New York, 1997.

63 (a) M. Toganoh and H. Furuta, *Chem. Commun.*, 2012, **48**, 937; (b) M. Toganoh and H. Furuta in *Handbook of Porphyrin Science*, eds. K. M. Kadish, K. M. Smith and R. Guilard, World Scientific, Singapore, 2010, pp. 295-367.

64 P. J. Chmielewski and L. Latos-Grażyński, *Coord. Chem. Rev.*, 2005, **249**, 2510.

65 (a) Y. Xie, T. Morimoto and H. Furuta, *Angew. Chem. Int. Ed.*, 2006, **45**, 6907; (b) A. Basu, M. Kitamura, S. Mori, M. Ishida, Y. Xie and H. Furuta, *J. Porphyrins Phthalocyanines*, 2015, **19**, 361.

66 L. Li, L. Wang, H. Tang and D. Cao, *Chem. Commun.*, 2017, **53**, 8352.

67 (a) S. Huang, R. K. Kannadorai, Y. Chen, Q. Liu and M. Wang, *Chem. Commun.*, 2015, **51**, 4223; (b) K. Li and B. Liu, *Chem. Soc. Rev.*, 2014, **43**, 6570.

68 M. Pawlicki, H. A. Collins, R. G. Denning and H. L. Anderson, *Angew. Chem. Int. Ed.*, 2009, **48**, 3244.

69 H. M. Kim and B. R. Cho, *Chem. Commun.*, 2009, 153.

70 Y. Chen, R. Guan, C. Zhang, J. Huang, L. Ji and H. Chao, *Coord. Chem. Rev.*, 2016, **310**, 16.

71 Y. Zhou, C. Ma, N. Gao, Q. Wang, P.-C. Lo, K. S. Wong, Q.-H. Xu, T. Kinoshita and D. K. P. Ng, *J. Mater. Chem. B*, 2018, **6**, 5570.

72 N. S. Makarov, M. Drobizhev and A. Rebane, *Opt. Express*, 2008, **16**, 4029.

73 O. Vakuliuk, A. Purc, G. Clermont, M. Blanchard-Desce and D. T. Gryko, *ChemPhotoChem*, 2017, **1**, 243.

74 S. Tang, E. H. Ghazvini Zadeh, B. Kim, N. T. Toomey, M. V. Bondar and K. D. Belfield, *Org. Biomol. Chem.*, 2017, **15**, 6511.

75 C. Kim, C. Favazza and L. V. Wang, *Chem. Rev.*, 2010, **110**, 2756.

76 V. Ntziachristos and D. Razansky, *Chem. Rev.*, 2010, **110**, 2783.

77 K. Miki, A. Enomoto, T. Inoue, T. Nabeshima, S. Saino, S. Shimizu, H. Matsuoka and K. Ohe, *Biomacromolecules*, 2017, **18**, 249.

78 (a) S. Saino, M. Saikawa, T. Nakamura, M. Yamamura and T. Nabeshima, *Tetrahedron Lett.*, 2016, **57**, 1629; (b) N. Sakamoto, C. Ikeda, M. Yamamura and T. Nabeshima, *Chem. Commun.*, 2012, **48**, 4818.

79 K. Miki, T. Inoue, Y. Kobayashi, K. Nakano, H. Matsuoka, F. Yamauchi, T. Yano and K. Ohe, *Biomacromolecules*, 2015, **16**, 219.

80 C. Wu, X. Huang, Y. Tang, W. Xiao, L. Sun, J. Shao and X. Dong, *Chem. Commun.*, 2019, **55**, 790.

81 Y. Yuan, Z. Wang, P. Cai, J. Liu, L.-D. Liao, M. Hong, X. Chen, N. Thakor and B. Liu, *Nanoscale*, 2015, **7**, 3067.

82 M. Zhang and R. Jin, *RSC Advances*, 2018, **8**, 33659.

83 A. Saeki, Y. Koizumi, T. Aida and S. Seki, *Acc. Chem. Res.*, 2012, **45**, 1193.

84 (a) W. Zhang, W. Jin, T. Fukushima, A. Saeki, S. Seki and T. Aida, *Science*, 2011, **334**, 340; (b) A. Saeki, M. Tsuji and S. Seki, *Adv. Energy Mater.*, 2011, **1**, 661.

85 A. Saeki, S. Yoshikawa, M. Tsuji, Y. Koizumi, M. Ide, C. Vijayakumar and S. Seki, *J. Am. Chem. Soc.*, 2012, **134**, 19035.